VII Zw 403: H I Structure in a Blue Compact Dwarf Galaxy

Caroline E. Simpson

Department of Physics, Florida International University, Miami, Florida 33199 USA

simpsonc@galaxy.fiu.edu

Deidre A. Hunter

Lowell Observatory, 1400 West Mars Hill Road, Flagstaff, Arizona 86001 USA

Tyler E. Nordgren

Department of Physics, University of Redlands, 1200 East Colton Avenue, Redlands, CA 92373 USA

Elias Brinks

Centre for Astrophysics Research, University of Hertfordshire, Hatfield AL 10 9AB UK

Bruce G. Elmegreen

IBM T. J. Watson Research Center, PO Box 218, Yorktown Heights, New York 10598 USA

Trisha Ashley

Department of Physics, Florida International University, Miami, Florida 33199 USA

Roger Lynds

Kitt Peak National Observatory, NOAO, Box 26732, Tucson, AZ 85726 USA

Vince J. McIntyre

Australia Telescope National Facility, CSIRO, P.O. Box 76, Epping, NSW 1710, Australia

Earl J. O'Neil

Kitt Peak National Observatory, NOAO, Box 26732, Tucson, AZ 85726 USA

Göran Östlin

Stockholm Observatory, Department of Astronomy, AlbaNova, SE-10691, Stockholm, Sweden

David J. Westpfahl

Department of Physics, New Mexico Institute of Mining and Technology, Socorro, NM 87801 USA

Eric M. Wilcots

Washburn Observatory, University of Wisconsin, 475 N. Charter St., Madison, Wisconsin 53706 USA

ABSTRACT

We present optical ($UBVJ$), ultraviolet (FUV, NUV), and high resolution atomic hydrogen (H I) observations of the nearby blue compact dwarf (BCD), VII Zw 403. We find that VII Zw 403 has a relatively high H I mass-to-light ratio for a BCD. The rotation velocity is nominally $10 - 15$ km s^{-1}, but rises to ~ 20 km s^{-1} after correction for the $\sim 8 - 10$ km s^{-1} random motions present in the gas. The velocity field is complex; including a variation in the position angle of the major axis going from the NE to the SW parts of the galaxy. Our high resolution H I maps reveal structure in the central gas, including a large, low-density H I depression or hole between the southern and northern halves of the galaxy, coincident with an unresolved x-ray source.

Although interactions have been proposed as the triggering mechanism for the vigorous star formation occurring in BCDs, VII Zw 403 does not seem to have been tidally triggered by an external interaction, as we have found no nearby possible perturbers. It also doesn't appear to fall in the set of galaxies that exhibit a strong central mass density concentration, as its optical scale length is large in comparison to similar systems. However, there are some features that are compatible with an accretion event: optical/H I axis misalignment, a change in position angle of the kinematic axis, and a complex velocity field.

Subject headings: galaxies: irregular — galaxies: star formation — galaxies: individual: VII Zw 403 — galaxies: ISM

1. Introduction

VII Zw 403 is classified as a blue compact dwarf (BCD) galaxy. Compact galaxies were first identified by Zwicky (1964) as high surface brightness objects that were just distinguishable from stars on the Palomar Sky Survey. This original classification included galaxies with a wide range of colors and total luminosities. Later, Thuan & Martin (1981) presented a study of 115 blue compact dwarf galaxies, which they defined as low luminosity ($M_B \leq -18$) galaxies with a compact optical size ($\lesssim 1$ kpc in diameter), that have optical spectra with "strong sharp narrow emission lines superposed on a blue continuum." The last two properties were chosen to ensure that the objects in their study had dense regions with active star formation.

It was shown early on that BCD galaxies could not have maintained such vigorous star formation for long periods of time (Searle & Sargent 1972), so such activity must be episodic. The cause of this activity is unclear. Unlike spiral galaxies, triggering mechanisms such as spiral density waves and shear are not present in dwarf galaxies, which tend to be slow, mostly solid-body rotators. Gravitational instabilities in the gas, which work well to predict the location of star formation in large galaxies, seem to work differently in dwarfs, where the average gas density is typically below the critical Kennicutt (1989) value by a factor of 2 or 3, and yet, stars still form.

Hunter & Elmegreen (2004) showed that the nature of the H II regions in BCDs are not that different from those in Ims; they are just crowded more closely together towards the center in the BCD galaxies. The amount of star formation caused by pressurized triggering versus spontaneous instabilities is likely similar as well. So what causes the centralized star formation bursts that characterize BCDs? Two possibilities explored in this paper include an inherent central mass density concentration (Salzer et al. 1999; van Zee et al. 2001) or gravitational interactions with nearby objects, including gas infall/accretion (Taylor 1997; Pustilnik et al. 2001; Hunter & Elmegreen 2004; Brosch et al. 2004).

Although gravitational interactions are often invoked to explain bursts of star formation in galaxies, previous studies have shown that not all the star formation activity in BCDs can be explained by external gravitational triggers. A plot of current normalized star formation rate vs. distance to the nearest projected (catalogued) galaxy (see Figure 14 in Hunter & Elmegreen 2004) shows no obvious correlation between presence/distance to companion and star formation activity for Ims, BCDs, or Sms in a sample of 140 galaxies. This is consistent with other searches for bright companions (Campos-Aguilar & Moles 1991; Telles & Terlevich 1995; Telles & Maddox 2000), and with work done by Brosch et al. (2004). This does not rule out possible triggering by much fainter companions, though, and there is some evidence for an excess of small/faint companions to BCDs (Taylor 1997;

Pustilnik et al. 2001), and there are several examples of BCDs with nearby small galaxies or gas clouds (e.g. Putman et al. 1998; Pustilnik et al. 2003). Such faint companions are difficult to detect and may have been missed in earlier studies of BCDs. As pointed out by Hunter & Elmegreen (2004), dwarf galaxies are common so "the most likely object to perturb any galaxy is a dwarf," but the effect of a small/faint companion on a nearby dwarf galaxy will be more dramatic than on a much larger system. They suggest that a possible mechanism for driving mass inflow in dwarfs would be perturbation by a small companion, resulting in angular momentum redistribution, and that such interactions could have happened long ago. Once a low angular momentum system is created, it can continue to host episodic star formation for long time periods (e.g. van Zee et al. 2001).

There is some evidence for central mass density concentration in BCDs in both the neutral gas (Taylor et al. 1994, 1995; van Zee et al. 1998; Simpson & Gottesman 2000) and in the optical underlying host galaxy (Papaderos et al. 1996a,b; Salzer et al. 1999). Van Zee et al. (2001) find that the 6 BCDS in their sample have steep rotation curves relative to low surface brightness dwarfs (LSBDs) with similar luminosities, with their mass distributions (stars, gas, and dark matter) more centrally concentrated, and that they are lower angular momentum systems than similar LSBDs. They suggest that it is just such low angular momentum systems that are able to collapse into centrally concentrated objects with high central densities. For a solid body rotation curve, the star formation threshold density is proportional to the slope of the rotation curve in a Toomre disk instability analysis (Toomre 1964). Hence, a steep rotation curve raises the critical threshold density for star formation. This delays the onset of star formation until the gas densities are quite high; and once star formation does begin, the system is more susceptible to bursting behavior than a more diffuse (higher angular momentum) system.

Another possible cause for the star formation activity that characterizes BCDs is the accretion/merger of a small gas cloud. Such events have been invoked to explain mismatches between the optical and (gas) kinematic axes in galaxies, twists in the velocity field, extended/unusual gas morphology (e.g. Hunter & Wilcots 2002), counter-rotation of the stellar and gas components, and the presence of stellar "shell" features in gas-poor systems (e.g. Coleman et al. 2004). Diagnosing the occurrence of a previous accretion/merger event in dIrr galaxies, however, is complicated by their low gravitational potentials, large gas fractions, and slow rotation. With slower rotation and low gravitational potentials, their velocity fields are more easily disturbed by the energy injection from star formation regions, for example.

As part of a project to determine what regulates star formation in small galaxies (Hunter & Elmegreen 2004, 2006), we have obtained multiwavelength data (UBV and Hα images) for 136 galaxies, with additional data (e.g. JHK, NUV, FUV) for a subset. These

data have recently been augmented by deep, high resolution interferometric atomic hydrogen spectral line (H I) observations of 40 of these galaxies as part of the LITTLE THINGS (LT) project: Local Irregulars That Trace Luminosity Extremes: The H I Nearby Galaxy Survey (http://www.lowell.edu/users/dah/littlethings/). As part of our investigation into star formation in dwarf galaxies, we are interested in looking at "what goes wrong" in BCDs—why they have such strong central star formation occurring. VII Zw 403 is one of a few BCD galaxies in our sample, and we use it here as a case study for actively star-forming dwarfs. Because it is apparently relatively isolated, with no spiral density waves or shear, it is a good testbed for examining how star formation might be triggered in active dwarf galaxies. We present the results of an initial study here; future papers associated with the LT project will present more in-depth analysis and modeling, particularly of the kinematics.

Although VII Zw 403 has generally been assumed to be a member of the M81 group, Karachentsev et al. (2002) state that VII Zw 403, with a distance of 4.4 Mpc, is behind the M81 group and is being accelerated towards both it and the Local Group. They find that VII Zw 403 is 1.14 Mpc from M81 and that the M81 group has a zero-velocity radius of 1.05 ± 0.07 Mpc. Lynds et al. (1998) and Schulte-Ladbeck et al. (1999) determined a distance of 4.5 Mpc using the tip of the red giant branch from color-magnitude diagrams based on *Hubble Space Telescope* (HST) data. This places it on the far side of the M81 group. Hunter & Elmegreen (2004) used the NASA/IPAC Extragalactic Database (NED)[1] to search for nearby galaxies in the plane of the sky within 1 Mpc and ±150 km s^{-1}. The only object found (an Im galaxy, KDG 073) had a projected distance of 900 kpc with a velocity difference of -32 km s^{-1}.

Loose & Thuan (1985) classified VII Zw 403 as an iE galaxy: one with irregular bright star formation regions near, but not at the center of, a low-surface brightness envelope. Subsequent observations with HST confirmed the presence of a smooth elliptical distribution of old, metal-poor red giant stars with an exponential fall-off in surface density (Lynds et al. 1998; Schulte-Ladbeck et al. 1999, and references therein). The scale-length for this evolved population is about 1 kpc (Lynds et al. 1998), which is normal for BCDs (Papaderos et al. 1996a). There are several bright H II regions with young blue stars loosely clustered nearby, and diffuse Hα emission as well. Fabry-Perot Hα maps (Thuan et al. 1987) detected little rotation, finding only a chaotic velocity field and a velocity dispersion of approximately 30 km s^{-1} in the diffuse emission, consistent with stellar winds.

Initial H I inteferometric observations by Thuan et al. (2004) revealed that although the H I is centrally concentrated in general in the galaxy, there are two areas of higher

---

[1]http://nedwww.ipac.caltech.edu/

flux density. The velocity dispersion map showed high values for the region separating the two peaks, and they interpret the high dispersion in the region between the peaks as due to a lack of flux. As most H I observations of BCDs show smoothly distributed gas with only one mostly centralized density peak, the presence of two peaks was intriguing, especially if truly separated by a region of lower density. To examine the gas morphology and kinematics in greater detail, and to search for possible companions and/or evidence of gravitational interactions, we subsequently obtained high spatial and velocity resolution H I interferometric data of VII Zw 403 to combine with multiwavelength optical, UV, and IR data. These data are presented below.

2.   The Observations

We have collected images of VII Zw 403 at a variety of wavelengths: Hα, *GALEX* FUV and NUV, ground-based $UBVJ$, and *Spitzer* 3.6 μm. The images are shown in Figure 1 and observations and data reduction are described below.

2.1.   Optical Images

We obtained UBV and Hα images of VII Zw 403 with the Perkins 1.8 m telescope at Lowell Observatory. The UBV images were obtained on photometric nights with a SITe 2048×2048 CCD binned 2×2 for a field of view of 10.4$'$. The V and B-band images were obtained on UT 13 March 1999 and the U-band image on 10 April 1999. The exposure times were 3×900 s for V, 4×1800 s for B, and 3×1800 s for U. The binned pixel scale was 0$''$608, and the seeing on individual and in the final averaged images was 2$''$1 in V, 2$''$8 in B, and 3$''$5 in U.

The data were reduced using common routines in Image Reduction and Analysis Facility (IRAF). Using CCDPROC, we subtracted the electronic pedestal (sometimes referred to as the "bias") using the overscan strip, and flat-fielded the images using twilight sky flats. Twilight flats were found, empirically, to work better than dome flats in removing large-scale structure in the CCD response. We used Landolt (1992) standard stars in 18 fields over the 3-night observing run in March 1999 to calibrate the BV photometry and in 13 fields over the 2-night observing run in April 1999 to calibrate the U-band photometry. The rms of the color terms were 0.015 mag for B, 0.009 mag for V, and 0.011 mag for U. The rms of the zero point terms were 0.015 mag for B, 0.088 mag for V, and 0.002 mag for U. The rms of the extinction coefficients were 0.045 mag for B, 0.053 mag for V, and 0.005 mag

for U. The images in each filter were averaged (IMCOMBINE) in such a way as to eliminate cosmic rays while still preserving the photometric integrity of the image. Specifically, images were compared pixel by pixel for values that deviated from the average by more than 3 sigma, based on the CCD noise characteristics. Deviant pixels were then eliminated from the average.

To prepare the images for surface photometry, we edited (IMEDIT) foreground stars and background galaxies from the final UBV images. The editing involved replacing a circular or rectangular area with an interpolation across the region based on the surroundings. The V-band image was done by hand, and then the cursor log file produced from that was used to remove objects from the other two filters. In that way, stars were removed in the same way for each filter. We then made a two-dimensional fit to the background (IMSURFIT) using the non-galaxy part of the image as seen in a deep display of the image. We subtracted (IMARITH) this sky image from the object image to produce a sky-subtracted final image for analysis.

We obtained Hα images of VII Zw 403 on 4 February 1995 using a TI 800 $\times$ 800 CCD provided to Lowell Observatory by the National Science Foundation. We used the Ohio State University Fabry-Perot as a simple 3:1 focal reducer since we were not interested in narrow-band spectral information and the Hα filter had a higher efficiency than the Fabry-Perot etalon. The Hα filter has a central wavelength of 6566 Å and a FWHM of 32 Å. The contribution from stellar continuum was determined using an off-band filter centered at 6440 Å with a FWHM of 95 Å. The Hα observations consisted of two 1300 s images, preceded and followed by a 600 s off-band observation. Given the FWHM of the filters, this approximately matched the S/N of the on and off-band filters. The pixel scale was $0''.49$, and the seeing on the individual and final image is $1''.7$. The electronic pedestal ("bias") was subtracted using the overscan strip, and the images were flat-fielded using dome flats.

We shifted, scaled, and subtracted the off-band image from the Hα image to remove the stellar continuum and leave only Hα nebular emission. We calibrated the Hα flux using observations of 5 spectrophotometric standard stars (Oke 1974; Stone 1977) and observations of the NGC 2363 nebula (Kennicutt et al. 1980) taken over the course of the 6-night observing run. These two types of calibrations agreed with each other to within 4%. The Hα flux has been corrected for the shift of the bandpass with temperature. The central wavelength shifts blueward by 0.018 nm for each degree of temperature decrease from 20° C, and so this needs to be considered in calibrating the flux through these narrow-band filters as it sometimes moves the object emission line off the peak of the transmission function. The Hα flux has also been corrected for contamination by the [NII]λ6584 emission line in the bandpass (a 1% correction).

2.2. Near-IR Image

We obtained the J-band image of VII Zw 403 with the Perkins 1.8 m telescope at Lowell Observatory with the Ohio State Infrared Imager-Spectrograph (OSIRIS DePoy et al. 1993) on the photometric night of UT 2 June 1996. The instrument consisted of four mosaiced detectors to create a total array of 256×256 pixels with a field of view of $6.4'$. The telescope was nodded to place VII Zw 403 first in one half of the array and then in the other half, so that sky could also be measured in the half without the galaxy. The galaxy was offset a few arcseconds between images in order to allow removal of hot pixels when the frames were averaged later. The image of VII Zw 403 is a combination of 48 exposures of 26 s each. The pixel scale was $1''.50$, and the seeing of the final image was $3''.2$.

The data were reduced in IRAF. Zero second bias frames were subtracted from all of the data, the image pixel values were corrected for non-linearity effects, and pixel to pixel sensitivity variations were removed using observations of a white screen in the dome. The non-linearity corrections were determined using a series of dome flats of increasing exposure time, to 29 seconds in steps of 1 second, sandwiched between darks.

Eight UKIRT standard stars from the list compiled by S. Courteau (1996, private communication) were used to calibrate the photometry. Each star was observed 4 times with the star placed in each quadrant in turn, and sky for a specific observation was taken from the observations with the star in the other quadrants. The rms of the zero point of the J-band calibration was 0.12 mag and of the extinction term was 0.08 mag. The California Institute of Technology (CIT) photometric system is 8% bluer in $J - H$ and 4% bluer in $H - K$ compared to the UKIRT system. The star forming region of VII Zw 403 shows up faintly on the Two Micron All Sky Survey (2MASS Skrutskie et al. 2006) J-band image: aJ_asky_990319n0730056.fits. On the 2MASS image, the flux in a $22''$ radius aperture centered on the star-forming regions has a magnitude of 13.73 ± 0.06. Our J-band image gives 13.71 ± 0.01. In spite of the difference in calibration systems (2MASS defines their own system), the magnitudes are the same within the uncertainties.

2.3. Ultraviolet Data

We obtained near-UV (NUV) and far-UV (FUV) images of VII Zw 403 from the *Galaxy Evolution Explorer* (*GALEX*) archives[2]. The images were part of the Nearby Galaxy Survey.

The FUV filter has a bandpass of 1350–1750 Å, an effective wavelength of 1516 Å, and a resolution of 4″.0. The FUV exposure time was 1617 s. The NUV filter has a bandpass of 1750–2800 Å, an effective wavelength of 2267 Å, and a resolution of 5″.6. The NUV integration time was 1479 s. The images were processed through the *GALEX* GR2/3 pipeline and were retrieved as final intensity maps with a 1″.5 pixel scale. The *GALEX* field of view is a circle with 1°.2 diameter, and we extracted a portion around VII Zw 403. We subtracted (IMEDIT) or masked foreground stars and background galaxies, and subtracted a low order two-dimensional fit to the background (IMSURFIT). The decision of what objects did not belong to the galaxy and should be removed was based on morphology (extended or stellar profiles), color, and similarity with other objects in the field well beyond the galaxy itself.

2.4. 3.6 μm Data

For completeness and to facilitate comparison, we include the 3.6 μm image taken of VII Zw 403 with the InfraRed Array Camera (IRAC Fazio et al. 1982) on the *Spitzer Space Telescope* (*Spitzer*). The data were obtained from the *Spitzer* archive and reduced with the Basic Calibrated Data pipeline. The full treatment of the data is described by Hunter et al. (2006).

2.5. H I Data

21 cm spectral line observations of the galaxy were made using the B, C, and D configurations of the NRAO[3]. Very Large Array (VLA). The B and D-configuration data were taken by Deidre Hunter; the C configuration by Trinh X. Thuan (proposal code AH0453), who kindly supplied us with these observations. The D configuration, with its short spacings, provides high sensitivity but a relatively low spatial resolution of $\sim 1'$. The C and B configurations, with longer baselines, provide higher resolution (nominally 12″.5 and 4″, respectively) but lower surface brightness sensitivity. After editing and calibration (discussed below), the three data sets were combined to produce images with both high sensitivity and high angular resolution.

Time on source for the C and D configuration observations was approximately 4 hours each; for the B, approximately 9 hours. Observations for all configurations were made using

---

[3]The National Radio Astronomy Observatory is a facility of the National Science Foundation operated under cooperative agreement by Associated Universities, Inc.

a correlator setting using 2IF mode with Hanning smoothing with a total bandwidth of 1.56 MHz. This results in 128 channels with a channel separation of 12.2 kHz (2.6 km s^{-1}). For spectral line data that are taken using on-line Hanning smoothing, the velocity resolution is equal to the channel separation, and so is also 2.6 km s^{-1}. Observational information is provided in Table 1.

The D configuration observations were set up to be consistent with the previously existing C configuration observations, so the two sets of observations could be combined after calibration for analysis. The central observing frequencies and velocities were the same, other than the usual changes in sky frequency due to the day, time, and location of the sources on the sky. However, the B configuration observations were taken during the beginning of the transition of the VLA to the Extended VLA (EVLA); so doppler tracking while observing was not available. The observations were done at a fixed frequency which corresponded with the central velocity (-60 km s^{-1}) from the C and D observations to within 3 or 4 channels (approximately 12 kHz). Before the B data were combined with the other two data sets (see below), the AIPS task CVEL was used to shift the spectra in the B data set to correct for the Earth's rotation and motion. Careful comparison of the resulting spectrum after applying CVEL with those from the C and D data ensured that all three data sets were now consistent in frequency and velocity space.

2.5.1. Calibration

Calibration of all three data sets was performed independently, using the standard routines in AIPS. For the D configuration data, the flux and bandpass calibrator was 1411+522 (3C 295; all sources are in J2000) and the phase calibrator was 1435+760 (J2000). The C configuration observations used 1044+809 for phase calibration and 1331+305 (3C 286) for the flux and bandpass calibration. The phase calibrator for the B configuration data was the same as for the D (1435+760), and the flux and bandpass calibrator was 0137+331 (3C 48).

The data reduction process was complicated by the presence of both absorption and emission from the Milky Way as VII Zw 403's systemic velocity is ~ -100 km s^{-1}. The single-dish spectrum (Figure 2) from the Greenbank 91m telescope (Thuan & Martin 1981) shows a broad absorption feature from ~ -55 to -30 km s^{-1}, with a strong emission feature from -30 to $\sim +5$ km s^{-1}. That emission feature shows a dip due to a narrow absorption line at a velocity of about 0 km s^{-1}.

To reduce the amount of data potentially contaminated by Galactic H I in the D configu-

ration calibrator data, a pseudo-continuum "channel 0" dataset was constructed by averaging together the inner 50% of the line data (normally, the inner 75% is used). This probably did not remove all the emission from the Milky Way, but was the best compromise given the situation. Because these were daytime observations, solar contamination was also present on the shortest baselines for the calibrators as well as for the source data. The affected short baselines for the calibrator data were not used during the calibration by the application of an appropriately chosen "uvrange" (only baselines longer than 0.55 k$lambda$ were used). Once a satisfactory calibration was achieved, it was applied to the source line data. The band-pass calibrator was only affected by Milky Way H I in a few channels, and as those hadn't stood out as unusual in the previous solutions, the bandpass calibration was done, again applying the uvrange limit (0.55 kλ) for the solar contamination. The continuum emission was removed using UVLIN, which does a linear fit to specified (line-free) channels and then subtracts the fitted baseline from the spectral line channels. The channels used for the fit were chosen to be free of both line emission and Galactic contamination.

For the C configuration observations, the continuum source 1331+305 (J2000) was observed for use as a flux and bandpass calibrator; the nearby continuum source 1044+809 (J2000) was observed for phase calibration. There was little Galactic or solar contamination present in these data. For the C data, calibration proceeded normally. During editing of the channel 0 source data, amplitudes above 0.4 Jy were clipped to remove anomalously high amplitude visibilities on the shortest baselines during the beginning of the observation run. The editing and calibration tables were copied over to the line data, and a dirty map of the source data was made to check for interference and look for line-free channels to use for continuum subtraction. Continuum subtraction using the line and inteference-free channels thus identified was done in the u-v plane using the task UVLSF, which works similarly to UVLIN.

The B configuration observations used 1331+305 (J2000) for flux and bandpass calibration, and 1435+760 (J2000) for phase calibration. The data from four antennas were flagged as unusable during the data collection process due to EVLA testing; four more antennas were not in use during the observations. During calibration, several large phase jumps in the phase calibrator data, on the order of 100 degrees, were observed for some of the antennas. All of these jumps occurred between scans near the end of the observing run. Changing the reference antenna for the calibration did not change the number or magnitude of the problematic jumps. After further consideration and testing, the galaxy source data from the scans that were in between the calibrator scans with phase jumps larger than 40 degrees were removed by flagging. Careful examination of the resulting images revealed no artifacts that would indicate phase errors with the data, such as asymmetric stripes, rings, or other odd-looking features. Self-calibration was also tried, but the resulting images were essen-

tially identical to those from the edited data. Results here are from the edited data that were not self-calibrated. As with the D data, continuum subtraction was done in the u-v plane using UVLIN. There was no apparent contamination from Milky Way emission visible in the B configuration data.

To check the calibration and data quality, the data from all three configurations were imaged separately using the task IMAGR, which uses a fast-fourier transform to create a cube of images, one image for each frequency (velocity) channel. During imaging, the effects of side-lobes of the non-gaussian features of the "dirty" beam were removed using the CLEAN algorithm (with a flux cut-off equal to the r.m.s. in a line-free channel). With the exception of the Galactic contamination obvious in the D configuration data (and faintly in a few channels of the C data), all three data sets were deemed acceptable.

A spectrum from our D configuration data (uniform weighting, with a ROBUST factor of +1)[4] is shown in Figure 3. Some of the Galactic contamination is strongly visible around 0 km s^{-1}, which doesn't overlap with VII Zw 403's emission, visible around -100 km s^{-1}. Many of the same features are present here as are in the Thuan & Martin (1981) single-dish spectrum, although at different levels. Presumably this is due to the spatial scale of the features; the D configuration is "blind" to structures larger than about $15'$ per spectral channel.

The D configuration data were then reimaged using natural weighting to emphasize faint emission; the spatial resolution is $72\rlap{.}''9 \times 53\rlap{.}''6$ and the 1σ noise in a single channel is 0.93 mJy beam^{-1} (see Table 1). Our integrated flux from the D configuration data is 11.5 Jy km s^{-1}, which is 25% lower than previous single-dish measurements. (We did not correct for the sensitivity fall-off of the primary beam, as the maximum extent of H I emission was approximately $6'$, which is well within the $30'$ full-width at half-maximum (FWHM) of the primary beam at 21cm.) Estimates from single dish observations are 14.6 (Huchtmeier & Richter 1986), 15.8 (Thuan & Martin 1981), and 16.2 Jy km s^{-1} (Huchtmeier & Richter 1989). We checked our flux calibration by comparing the fluxes of continuum sources from our data to the catalogued fluxes listed in the NRAO VLA Sky Survey (NVSS[5]; Condon et al. (1998)). There are two catalogued continuum sources close ($3.7'$ and $3.5'$) to the galaxy; our measured fluxes are 79% and 76% of the NVSS fluxes, respectively. If we adjust our D configuration integrated flux by 20%, this still only comes to 13.8 Jy km s^{-1}. A comparison of a spectrum

---

[4]The ROBUST parameter allows the user to choose a weighting scheme between fully uniform (-5) and fully natural ($+5$). This produces images with either higher spatial resolution but poorer signal-to-noise (fully uniform) or lower spatial resolution but higher signal-to-noise (fully natural).

[5]http://www.cv.nrao.edu/nvss/

through the D configuration data cube restricted in area to the spatial extent of the galaxy on the sky is shown in Figure 4, along with the single-dish spectrum from Thuan & Martin (1981). Presumably, all the single-dish integrated fluxes include the second emission peak located at about -70 km s^{-1}. We have determined that this secondary emission peak is almost certainly from the Milky Way, not VII Zw 403 itself. Comparing just the emission from VII Zw 403, it is clear that our observations have detected all of the flux seen in the single-dish spectrum.

This is a different conclusion than that reached by Thuan et al. (2004). They present the VLA C configuration data that we show here, but did not have the D configuration data and so were not aware of the Galactic emission in the field of view. They also present a comparison of their C data spectrum to the original Thuan & Martin (1981) single-dish spectrum. Their C spectrum resembles our D spectrum without the Milky Way emission; indeed their total integrated flux from the C configuration data is 11.0 Jy km s^{-1}, which is close to our 11.5 Jy km s^{-1} value. However, without knowing that the single-dish flux included the Galactic emission as well, they were forced to conclude that their VLA data were missing some (presumably large-scale) emission from VII Zw 403.

2.5.2.   Imaging

Channel maps from part of the D configuration data cube are shown in Figure 5. The Galactic contamination is clearly visible in the channels from -23.9 to -78.0 km s^{-1}. Several of these channels also contain emission from VII Zw 403. Before integrating the cube to produce the moment maps showing the integrated flux, velocity field, and velocity dispersion, the affected channels were selectively blanked to remove the Galactic emission, leaving only the small region in the center of each field that contained emission from VII Zw 403. This partially blanked cube was then integrated in velocity using the channels from -60.0 to -147.5 km s^{-1} with the AIPS task MOMNT. To avoid integrating up noise as well as signal, MOMNT creates a mask cube smoothed in space (by convolving with a gaussian twice the size of the beam) and velocity (by hanning smoothing); pixels falling below the specified flux cutoff in the mask cube are then blanked in the original cube prior to integration. For this dataset, a flux cutoff of twice the single-channel r.m.s. was used. These moment maps were used for the analysis discussed in § 4.

To produce a data set with good sensitivity and enhanced but still moderate resolution, the data from the C and D configurations were combined in the u-v plane using the AIPS task DBCON and then imaged using the AIPS task IMAGR with a ROBUST weighting factor of $+1$ (we will refer to this cube as the C+D$_1$ cube). This weighting was chosen based on tests

to determine the best balance of resolution and flux recovery (sensitivity) for the purposes of velocity field analysis, primarily. Although the Galactic contamination wasn't as strongly present as in the D-configuration-only data, it was still present at high enough levels to warrant concern. We therefore blanked everything but the emission from VII Zw 403 (in the center of the field) in the eight affected channels before integrating. A flux cutoff of twice the single channel r.m.s (see Table 2) was used to produce the combined data moment maps. This data set was used for the velocity analysis and H I surface density analyses, below.

The data from all three configurations were also combined in the u-v plane and imaged. Galactic contamination was not detectable in any of the resulting data cubes, so no extra blanking was necessary. We tested a variety of ROBUST weighting factors while imaging to determine the best values to provide the desired resolutions while recovering the most flux possible for each resolution. After extensive testing and comparison, we created three data cubes with varying sensitivities and resolutions: a ROBUST of 0 produced a medium resolution data set (B+C+D_0) which was used to examine the morphology of the integrated flux (the first moment map); a ROBUST of +1 produced a lower resolution data set (B+C+D_1) used to analyze the velocity dispersion in the gas (the second moment map); and a ROBUST of -1 was used to create a high resolution (B+C+D_{-1}) image of the integrated flux in the highest density regions of the galaxy. Details (resolutions, noise levels) are given in Table 2.

3. The Optical View of the Galaxy

The images of VII Zw 403 are shown in Figure 1. The galaxy is elliptical-shaped with a moderate degree of ellipticity implying a relatively high inclination angle. At outer V-band isophote levels VII Zw 403 is quite symmetrical. However, at intermediate isophotes (radius 40–60″) there is an extension of stars to the north that is not mirrored to the south. This type of feature is seen in other irregulars as well, such as NGC 2366 (Hunter et al. 2001).

3.1. Broad-band Surface Photometry

From the V-band image, we determined the morphological center of the galaxy, b/a, and position angle of the major axis from a contour plot of the image block-averaged by 5 to increase the signal-to-noise in the outer parts. We used an outer contour corresponding to a μ_V, not corrected for reddening, of 27.2 mag arcsec^{-2}. The major axis and position angle were determined to be the long line of symmetry around which the galaxy could be folded. The center was the mid-point bisecting the isophote along the major and minor axes.

The center of the galaxy is at 11^{h} 24^{m} $33\rlap{.}''4$, $79°$ $16'$ $10''$ (B1950), with an uncertainty of $2''$ in each direction. We also determined the center of the galaxy from *Spitzer* IRAC 3.6 μm images (Hunter et al. 2006), with an estimated uncertainty of $3''$. The 3.6 μm center is offset from that of the V-band by $4''$ W and $3''$ N, and this then more realistically describes the uncertainty in the position of the center of the stellar body. Below we will derive the H I kinematic center as well. That center is at 11^{h} 24^{m} $35\rlap{.}^{\mathrm{s}}1\pm10\rlap{.}^{\mathrm{s}}3$, $79°$ $16'$ $18\pm27''$ (B1950). The H I kinematic center is offset from that of the V-band by $5''$ E and $8''$ N, well within the large error bars of the H I kinematic center. For the surface photometry we used the V-band morphological center. We measured the minor-to-major axis ratio b/a on the V-band image to be 0.49. Dwarf irregular galaxies are considered to be thicker than spiral disks and an intrinsic $(b/a)_0$ of 0.3 is suggested (Hodge & Hitchcock 1966; van den Bergh 1988; but see Sung et al. 1998). This b/a then implies an inclination of $66°$ for VII Zw 403. We measured the position angle of the major axis to be $-11°$.

The surface photometry (ELLIPSE in STSDAS) used 10 ellipses starting at a semi-major axis of $9''$ and progressing to $91''$ in steps of $9\rlap{.}''1$. All of the other images were geometrically transformed (GEOMAP, GEOTRAN) to match the V-band image and elliptical surface photometry was done identically on all images. The geometric transformation used stars identified in both the V-band image and the target image to determine the surface distortions necessary to make the target image have the same size, pixel scale, and orientation of the V-band image.

The surface photometry is collected in Figure 6. The surface photometry and colors have been corrected for reddening using a total $\mathrm{E}(B-V)_t{=}\mathrm{E}(B-V)_f{+}0.05$, where the foreground reddening $\mathrm{E}(B-V)_f$ is 0.023 (Burstein & Heiles 1984). An internal reddening of 0.05 in $\mathrm{E}(B-V)$ was used to be consistent with Balmer decrement measurements of H II regions in dIm galaxies. Hunter & Hoffman (1999) found an average $\mathrm{E}(B-V)$ of 0.1 for H II regions in 39 dIm galaxies. The stars outside of H II regions were taken to have a reddening of half of this value. We used Burstein and Heiles values for the foreground reddening rather than those of Schlegel et al. (1998) because the latter values are systematically higher than the former and some are inconsistent with Balmer decrement measurements. Our value of the reddening of the stars in VII Zw 403 is close to that of Lynds et al. (1998) who obtained an $\mathrm{E}(B-V)$ of 0.04–0.08 for stars and stellar associations from analysis of color-magnitude diagrams. We use the reddening law of Cardelli et al. (1989) and $A_V/\mathrm{E}(B-V){=}3.1$ for the optical, near-IR, and FUV reddening corrections. The NUV reddening is affected by the 2175 Å bump. For the NUV, we have adopted the reddening formula of Wyder et al. (2007).

We determined R_{25}, the radius at a B-band surface brightness of 25 mag arcsec^{-2}, to be $36\rlap{.}''5$ which is 0.78 kpc at the galaxy. Our radius is 10% smaller than that given by

de Vaucouleurs et al. (1991). The Holmberg radius, R_H, originally defined to a photographic surface brightness, is measured at an equivalent B-band surface brightness $\mu_B = 26.7 - 0.149(B - V)$. For our measured $(B - V)_0$ of 0.3, the Holmberg radius is determined at a μ_{B_0} of 26.66 magnitudes arcsec^{-2}. We find that R_H is 69″ which is 1.47 kpc at the galaxy. Both R_{25} and R_H are determined from the reddening corrected surface photometry. Integrated properties of VII Zw 403 are collected in Table 3.

We fit an exponential disk to the broad-band photometry beyond 0.2 kpc, and the fits to the V-band, 3.6 μm, and NUV data are shown in the upper panel of Figure 6. The outer disk of VII Zw 403 is fit well with an exponential disk profile having a central surface brightness μ_0^V of 22.94±0.09 magnitudes arcsec^{-2} and a disk scale length R_D^V of 0.50±0.01 kpc. Interior to a radius of 1.0 kpc, the surface brightness profile is steeper, although it too is fit well with an exponential disk with a disk scale length of 0.37±0.01 kpc. The 3.6 μm surface brightness profile follows the slope of the V-band reasonably well while the NUV profile is considerably steeper. The similarity between the V and the 3.6 μm profiles implies that the star formation as a function of radius integrated over a 1-Gyr time scale is the same as that integrated over the lifetime of the galaxy. The steeper NUV profile suggests that star formation over the last 200 Myrs has been concentrated to the center of the galaxy.

Surface brightness profiles of BCDs are generally found to contain multiple components with the outer component representing the galaxy underlying the intense current star formation (Papaderos et al. 1996b; Cairós et al. 2003; Noeske et al. 2003). The central portions of these galaxies, on the other hand, are dominated by the current star formation, and the profiles are often steeper or more complex there. Papaderos et al. (1996a) found that the scale-length of the outer disks of BCDs are smaller, by half on average, than those of Im galaxies. However, Hunter & Elmegreen (2006) find for a sample of 94 Im systems and 24 BCDs that the scale-lengths of the BCDs are only slightly offset (in the sense of shorter scale-length at comparable M_V) from those of most Im galaxies. It is the higher scale-length tail in the number distribution that is more drastically reduced for their BCD sample compared to dIms. Compared to these samples, VII Zw 403's scale-length lies at the peak in the distribution of dIms and BCDs.

Integrated colors of VII Zw 403 are given in Table 3. In a UBV color-color diagram for a large sample of Im, BCD, and Sm galaxies (Hunter & Elmegreen 2006), VII Zw 403 lies at the blue side of the range, clearly dominated by a young stellar population. On the other hand, the integrated $(V - J)_0$ places VII Zw 403 in the middle of the range shown by Im and BCDs in that color (Hunter & Elmegreen 2006).

Azimuthally-averaged radial profiles of the colors are shown in Figure 6. In most Im galaxies the azimuthally-averaged colors are generally constant over the disk of the galaxy;

irregular galaxies do not usually have color gradients. VII Zw 403, however, does show a gradient towards redder colors in the outer part of the galaxy. $(B - V)_0$ and $(U - B)_0$ track each other and change by about 0.5 mag from the center into the outer galaxy, beyond the Holmberg radius. We can only trace $(V - J)_0$ to 1.1 kpc, but it is approximately constant over this radial range. $(FUV - NUV)_0$ also is roughly constant throughout the optical galaxy to R_{25}. This trend in the colors is due to the fact that star formation is concentrated to the center of the galaxy. Stellar populations becoming redder as one goes outwards from the center is seen in many BCDs (Papaderos et al. 1996b; Cairós et al. 2003; Noeske et al. 2003).

We have modeled the UV and optical colors of VIIZw403's annular surface photometry using population synthesis fitting. These models use simple evolutionary histories and the stellar populations library of Bruzual & Charlot (2003). Details can be found in Hunter et al. (2010). We find that the colors of the central region (<0.5 kpc) is dominated by a stellar population with an age of about 400±200 Myrs, while the colors beyond that radius are fit with stellar populations of 1-3 Gyr of age.

3.2. Star-Forming Regions

Hα traces star formation over the past 10 Myr, and Figure 1 shows that most of the current star formation in VII Zw 403 is found in one large complex located 6″ east and 2″ north of the center of the galaxy, only 130 pc from the nominal center determined from the outer V-band isophote. This type of central concentration of star formation is often seen in Blue Compact Dwarfs, and is probably responsible for VII Zw 403's classification as a BCD.

We show the azimuthally-averaged Hα surface brightness in Figure 6. Although the current star formation in VII Zw 403 is contained in a giant H II complex at the galaxy center (the Hα emission seen in Figure 1), because the H II complex is large, Hα emission appears in elliptical annuli out to a radius of 1.3 kpc. The Hα surface brightness drops off faster than the starlight in the V-band and 3.6 μm image, dropping only a little faster beyond 0.75 kpc and ending at 1.3 kpc.

The FUV and NUV passbands measure the light directly from stars and are dominated by young massive stars formed over the past 200 Myr. Thus, the UV is sensitive to star formation over a longer timescale than Hα. In Figure 6 the UV profile, however, follows the Hα profile closely. Thus, the ultraviolet surface brightness profile is dominated by the same central star-forming event as we see in Hα (see Figure 1).

The integrated Hα and UV luminosities and derived star formation rates of the galaxy

are given in Table 3. The star formation rates derived from $L_{H\alpha}$ and the FUV luminosity use the formulae of Hunter et al. (2010) that integrates from 0.1 $M_\odot$ to 100 $M_\odot$ with a Salpeter (1955) stellar initial mass function. The star formation rate derived from Hα is similar to that derived from the UV. VII Zw 403 has a star formation rate per unit area that is normal, but towards the high end of the range, for irregular galaxies (Hunter & Elmegreen 2006), as shown in Figure 7. Again, this is consistent with the galaxy's classification as a BCD. However, modeling of the color-magnitude diagram of the stellar population by Lynds et al. (1998) suggests that the star formation rate was much higher about 600–800 Myr ago than it is today, by as much as a factor of 30.

The V and 3.6 μm-band radial profiles in Figure 6 are smooth exponential disks with about the same slope in the central part of the galaxy, but the Hα and NUV are peaked in the center and fall faster than V or 3.6 μm. This indicates a change in the primary site of star formation about 200 Myr ago, the timescale the NUV is sensitive to. This is a relatively short dynamical time ($\approx$ two galactic rotations; see § 4.3) for this slowly rotating galaxy. We cannot determine the cause of this shift in star formation location, but it is unlikely to have been caused by a collision or accretion event. The timescale is short enough that we should still see either two galactic nuclei or tidal debris, which we don't. A central collapse to a bar could explain it, but we see no hint of a bar in the V, J, or 3.6 μm images.

At its current rate of consumption, the galaxy can turn gas into stars for another 5 Gyr if all of the gas associated with the galaxy can be used. The timescale to run out of gas becomes 10 Gyr if recycling of gas from dying stars is also considered (Brinchmann et al. 2004). These timescales to exhaust the gas are somewhat short for irregular galaxies (Hunter & Elmegreen 2004), but nevertheless, the galaxy is in no danger of running out of the fuel for star formation any time soon.

4. H I Results

As H I is the raw material from which molecular clouds, and then stars, form, the H I properties of a galaxy are fundamental to understanding its past, current, and future star formation. The total H I mass from the integrated D configuration data is 5.23×10^7 $M_\odot$, which is below the median of 3.0×10^8 for the large sample of star-forming galaxies studied by Salzer et al. (2002). This value for the hydrogen mass includes only the emission we believe is associated with VII Zw 403 itself. This does not include the secondary emission peak seen in the spectrum around -70 km s^{-1} that we believe is due to Galactic contamination (see § 2.5.1).

The M_{HI}/L_B is 0.91. This is within the range (0.2–2.0) of the sample of 11 BCDs from van Zee et al. (1998, 2001), but is on the high end of the distribution for the 24 BCDs (~ 0.005 to ~ 1.8), and below the median for Ims (~ 1.3) shown in Figure 4 of Hunter & Elmegreen (2004). For comparison with the sample in Salzer et al. (2002), we follow their method to "correct" the global luminosity by removing the effect from the starburst so that it is more representative of the bulk of the stars in the galaxy. This increases the M_{HI}/L_B ratio to 1.82, which is higher than the Salzer et al. (2002) median of 1.3. Although the H I mass for VII Zw 403 is relatively low on an absolute scale, its relatively high M_{HI}/L_B (even "uncorrected" for the starburst) could indicate that it is either a somewhat gas-rich BCD or is currently "luminosity-poor" as it is presumably post-starburst: it should have been brighter during the burst of 600–800 Myr ago detected by Lynds et al. (1998).

4.1. H I Surface Density

The azimuthally averaged surface density profiles of the H I gas for VII Zw 403 using the center, position angle, and inclination from both the optical and H I data are shown in Figure 8. The profiles were calculated by integrating the H I from the C+D$_1$ map (beam size $34\rlap{.}''1 \times 27\rlap{.}''6$) using $30''$ rings with (1) a center position of $11^h24^s33\rlap{.}^s5$, $79° 16' 10\rlap{.}''3$ (B1950.0), a position angle of $-11°$, and an inclination of $66°$ taken from the V-band photometry (§ 3); and (2) a center position of $11^h24^s 35\rlap{.}^s1 \pm 10\rlap{.}^s3$, $79° 16' 18 \pm 27''$(B1950.0), a position angle of $47°$, and an inclination of $77°$ taken from the NE half of the H I rotation curve analysis (§4.3).

Several Im galaxies are also plotted in Figure 8. The galaxies were chosen to have similar linear resolutions in that the ratio of the beam size to either the disk scale length (R_D) or the half-light radius ($R_{1/2}$) is approximately the same. The ratios range from 1.1 to 2.4 for beam/R_D and 0.5 to 1 for beam/$R_{1/2}$. The values for VII Zw 403 are 1.4 and 1.2, respectively. We can see from the figure that the H I surface density for VII Zw 403 derived using the H I parameters falls off smoothly and slightly more steeply in the central regions than those for the Ims; more so when using the optical parameters. In comparison to the BCD and dIrr H I surface density profiles presented in van Zee et al. (1998), the shape of VII Zw 403's profile is similar to those of the BCDs, and somewhat steeper than those for the dIrrs. The central surface densities from both the optical and H I parameters for VII Zw 403 are seen to be low compared to the BCDs in the sample; when using the H I parameters, the central surface density is like that of the dIrrs.

4.2. Morphology

Figure 9 shows the integrated $C+D_1$ H I contours on the V image, with the contrast set to show the full extent of the galaxy's optical emission. This figure shows that there is a large, low-level irregular skirt of H I gas that extends beyond the optical emission, especially toward the south. Irregular gas distributions that extend beyond the optical emission, which are common in field galaxies, are also found in other BCDs (Taylor et al. 1994; van Zee et al. 1998, 2001; Thuan et al. 2004). From the D configuration data (not shown), the total extent (diameter) of the H I ($2R_{HI}$) out to the 1×10^{19} cm^{-2} level is $5'.24$ (deconvolved). This is 2.3 $R_{\rm H}$, which is typical for the Ims in Figure 13 of Hunter (1997).

At the spatial resolution of the $C+D_1$ image ($\sim 700 \times 600$ pc), the H I appears smoothly distributed with the density increasing toward the center of the galaxy. This smoothly increasing density is often seen in BCDs (Taylor et al. 1994; Simpson & Gottesman 2000; van Zee et al. 1998, 2001); and although some "clumpiness" of the H I is also seen in BCDs (van Zee et al. 1998), it is not like the highly-structured gas distribution often observed in dIrrs, where shells, filaments, and loops are frequently visible (Meurer et al. 1992; Puche et al. 1992; Young & Lo 1996; Martin 1998; Meurer et al. 1998; Walter & Brinks 1999; Stewart et al. 2000; Ott et al. 2001; Simpson et al. 2005a,b). Comparison of the H I distribution in VII Zw 403 to those in dIrrs with similar linear spatial resolution, such as DDO 88 (Simpson et al. 2005a) and DDO 43 (Simpson et al. 2005b), shows that at these scales, this increased "smoothness" in VII Zw 403 is real. Clumping of the H I on the scales seen in dIrrs is not visible in VII Zw 403.

At higher spatial resolution, however, some structure begins to be revealed in the H I. Figure 10 shows the integrated H I flux from the $B+C+D_0$ data cube, with a linear resolution of 200 $\times$160 pc ($9'' \times 8''$), as compared to the 750×600 pc resolution of the $C+D_1$ image. (Please note the change in field of view of the two images; the $B+C+D_0$ image shows only the inner $2'$, which corresponds roughly to the area covered by the central three contours in the $C+D_1$ map shown in Figure 9.) This image shows that the central H I distribution contains a region of lower density separating a large clump to the south of the center and a much smaller clump to the north, connected by a ridge on the west side. This low density region resembles a partial cavity or hole, with decreasing density to the east side. This is further discussed below.

4.3.   The Velocity Field

In Figure 11 we show the channel maps from the $C+D_1$ data cube that were integrated to produce the flux-weighted H I velocity field shown in Figure 12, and in Figure 13 as isovelocity contours superposed on the V-band image of VII Zw 403. One can see here that there is ordered rotation, with the NE portion of the galaxy approaching and the SW half of the galaxy receding. However, it is also immediately apparent that the velocity field is complex. First, there is a curve in the isovelocity contours so that the NE and SW portions of the galaxy have distinctly different kinematic axes. The kinematic axis of the NE half of the galaxy is aligned roughly at an angle of $+45°$. The SW part of the galaxy, on the other hand, appears to have a line of nodes at about $+25°$, which is aligned more closely with the optical galaxy's major axis at $-11°$. Second, there are places where the velocity field is not well behaved. In particular on the east side of the galaxy the isovelocity contours curve back upward in a complex manner, and in the south there are "islands" of different velocities.

As strange as this velocity field appears, there are other dwarf galaxies with curves in the position angles of their isovelocity contours similar to what we see in VII Zw 403. A review of the literature revealed ten other BCDs with this type of feature (ESO338-IG04: Östlin et al. 2001; Haro 2: Bravo-Alfaro et al. 2004; Haro 33, Mrk 51: Simpson & Gottesman 2000; NGC 1569: Stil & Israel 2002b; NGC 3738: Stil & Israel 2002a; NGC 1705: Meurer et al. 1998; UGC 4483, UM462: van Zee et al. 1998; UM323: van Zee et al. 2001), and there are undoubtedly others. However, this phenomenon is not exclusively that of BCDs. We also found a comparable number of Im galaxies with this sort of feature (DDO 22, DDO 68: Stil & Israel 2002a; DDO 69: Young & Lo 1996; DDO 165, DDO 187, UGC 3698: Swaters 1999; DDO 210: Begum & Chengalur 2004; DDO 216: Young et al. 2003; ESO 245-G005: Côté et al. 2000; NGC 2366: Hunter et al. 2001; NGC 4163: Simpson & Gottesman 2000). Since some of the Im galaxies have no current star formation activity or very little, we cannot associate this velocity field feature with the starburst that makes VII Zw 403 special. In addition, this is not relegated only to slow rotators, such as VII Zw 403. In the sample taken from the literature, maximum rotation speeds range from very small up to 69 km s^{-1}. Distortions in velocity fields are often blamed on gravitational interactions with other galaxies. In these galaxies, some are known to have small companions and others are not.

To get some idea of the rotation of VII Zw 403, using the task GAL in AIPS we fit the two halves of the velocity field separately and began with the NE or approaching half. We used the $C+D_1$ moment map which has a beam size of $34\rlap{.}''1 \times 27\rlap{.}''6$. With the H I peak as a first guess on the position of the kinematic center, we fit the field with a Brandt function (Brandt 1960). We also experimented with changing the initial conditions: we varied the position angle from $34–65°$, the inclination from $66°$ to $72°$, and maximum rotational velocity from 13

tp 15 km s^{-1}. We also varied the radial extent of the fit to raidd of 130$''$, 90$''$, and 75$''$; the center up to eight pixels; and the systemic velocity by a few km s^{-1}. We tried fitting the whole field and just one side at a time while varying initial parameters. For the final rotation curve(s) we used a position angle of 40°, an inclination of 66°, and a rotational velocity of 13 km s^{-1} for the initial guesses. From this we determined the center (11$^{\rm h}$ 24$^{\rm m}$ 35$\overset{\rm s}{.}$1±10$\overset{\rm s}{.}$3, 79° 16$'$ 18±27$''$, B1950.0) and systemic velocity (-103 ± 1 km s^{-1}). The experiments with varying initial guesses suggested that the uncertainties given above are reasonable. A fit with the center fixed and a solid body function yielded the same systemic velocity. We then fixed the center position and central velocity and fit the field in concentric rings that were 15$''$ in width and stepped every 15$''$. The innermost circle did not yield a solution and that point is omitted. For the SW or receding half of the galaxy, we adopted the center position and systemic velocity determined from the NE half and again fit in concentric rings.

The results are shown in Figure 14 as solid circles. The kinematic axis in each ring is traced as the black line on Figure 13. One can see that for each half alone the position angle is relatively stable with radius except for the outer two annuli on the SW side. The inclination, on the other hand, is quite variable although over much of each half of the field it changes systematically. Generally the inclinations are all higher than we expect based on the optical major-to-minor axis ratio. The maximum rotation speed is about 15 km s^{-1} on the NE side and a few km s^{-1} lower on the SW side.

With a maximum rotation velocity of only $\sim$15 km s^{-1} ($\sim$ 16 km s^{-1} when corrected for an inclination $i = 66°$) and an average dispersion velocity in the C+D$_1$ map of 8.5 km s^{-1} (Figure 15; §4.4), the galaxy has a significant amount of pressure support from the random motions in the gas. This means that simply using the rotation velocity will result in an underestimate of the dynamical mass. We have corrected for this by adding in the pressure support; this is called the asymmetric drift correction. To calculate this, we used the procedure described in Begum & Chengalur (2004) and we follow their discussion here. To make this applicable to a gas disk rather than a collisionless stellar system for which the rotational velocities are much larger than the random motions, we make the assumption that the pressure support can be approximated by the gas density times the square of the velocity dispersion:

$$v_c^2 = v_0^2 - r\sigma^2[\frac{\mathrm{d}}{\mathrm{d}r}(\ln\Sigma_{\rm HI}) + \frac{\mathrm{d}}{\mathrm{d}r}(\ln\sigma^2) - \frac{\mathrm{d}}{\mathrm{d}r}(\ln 2h_z)]. \tag{1}$$

Here, v_c is the corrected circular velocity, v_0 is the observed rotation velocity from the original rotation curve, $\Sigma_{\rm HI}$ is the H I surface density, σ is the velocity dispersion, and h_z is the scale height of the H I disk. We further assume that neither the velocity dispersions nor the scale height vary significantly across the disk (i.e. with radius r), so their derivatives are

zero, leaving us with

$$v_c^2 = v_0^2 - r\sigma^2 [\frac{\mathrm{d}}{\mathrm{d}r}(\ln \Sigma_{\mathrm{HI}})]. \tag{2}$$

To determine the derivative of the H I surface density, we must determine a functional expression to describe it. Towards this end, we fit the profile (derived using the optical center) shown in Figure 8 with a Gaussian of the form:

$$\Sigma_{\mathrm{HI}}(r) = \Sigma_0\, \mathrm{e}^{-(r-\mu)^2/2r_0^2} \tag{3}$$

where Σ_0 is the amplitude, μ is the radius at which the Gaussian peaks, and r_0 is the scale length. The profile was fairly well fit with $\Sigma_0 = 11.42 \pm 0.54\ M_\odot\ \mathrm{pc}^{-2}$, $\mu = 26 \pm 6''$ (0.55 kpc), and $r_0 = 57 \pm 3''$ (1.26 kpc). Taking the derivative, eq. 2 now becomes

$$v_c^2 = v_0^2 + \frac{r(r-\mu)\sigma^2}{r_0^2}. \tag{4}$$

Using the values found from the gaussian fit and a galaxy-wide average of 8.0 km s^{-1} as a conservative lower estimate for the velocity dispersion (corrected for observational broadening due to the velocity resolution), we then corrected the rotation curves for both the NE and SW halves. The result is shown in Figure 14 (open circles), along with the uncorrected rotation curves (solid circles). Applying the correction increases the maximum velocities to 20 km s^{-1} for the NE half and 22 km s^{-1} for the SW half. The corrected rotation curve is essentially that of a solid body on both sides of the galaxy.

The necessity of correcting the rotation to include pressure support is apparent when we calculate a dynamical mass for VII Zw 403. Using the highest rotational velocity from the uncorrected rotation curves and $M = V_{\mathrm{max}}^2 R_{\mathrm{max}}/G$ we get an estimated dynamical mass of $7.9 \times 10^7\ M_\odot$. This is an $M_{\mathrm{HI}}/M_{\mathrm{dyn}}$ of 0.66, which is higher than the ranges for BCDs found by others (Taylor et al. 1994; van Zee et al. 1998, 2001). The problem becomes worse when the total luminous mass ($M_{\mathrm{gas}} + M_{\mathrm{stars}}$) is considered. The gas mass is found by multiplying the H I mass by a factor of 1.34 to correct for He. No correction is made for molecular gas; no good estimates exist as CO detections in BCDs have been few, and those primarily in BCDs with elliptical inner isophotes (Sage et al. 1992), or in metal-rich dIrrs: Taylor et al. (1998) report from a literature sample that there are no known detections of CO in galaxies with $12 + \log(O/H) < 7.9$. VII Zw 403 has irregular inner isophotes and $12 + \log(O/H) = 7.69$ (Izotov & Thuan 1999), so is unlikely to have detectable CO.

To find the mass in stars, we can estimate a lower limit by using a stellar M/L_V ratio from Bell & de Jong (2001) that is a function of $(B - V)_0$ color: $\log(M/L_V) = -0.37 + 1.14(B - V)_0$. This is appropriate for a Salpeter (1955) stellar initial mass function and metallicity $Z = 0.008$ and is derived using the Bruzual & Charlot (2003) stellar population

models. This results in a stellar mass of approximately 3.9×10^7 $M_\odot$, or a stellar mass-to-light ratio of 0.89. However, this does not take the starburst into account. Assuming that the SFR was 30 times higher for 200 Myr (Lynds et al. 1998) during the past 13 Gyr, we then add that to the constant SFR model (0.013 $M_\odot$ yr^{-1}) and obtain an upper estimate of 9×10^7 $M_\odot$ (stellar $M/L_{\rm B} = 1.6$). With this range, our luminous mass estimate is between 1.1×10^8 and 1.6×10^8 $M_\odot$. Even the lower of these is greater than the highest dynamical mass estimated from the uncorrected rotation curve by a factor of 1.4.

However, when we use the corrected rotation curves to calculate a dynamical mass, we get $M_{\rm dyn} = 2.5 \times 10^8$ $M_\odot$, which is 1.5 times larger than even the higher estimate of the luminous mass. This is now a $M_{\rm HI}/M_{\rm dyn}$ of 0.21, which is more in line with those in Taylor et al. (1994) and van Zee et al. (1998, 2001).

4.4. Velocity Dispersions

Contours from the B+C+D$_1$ data showing the velocity dispersions across the galaxy overlaid on the H I flux map are shown in Figure 15. In general, the higher dispersion areas (~ 10 km s^{-1}) correspond to the area where most of the Hα flux originates, as shown in Figure 16. There is nothing notable in either the V or Hα images in the unresolved region of highest dispersion (located just NE of the large H I clump), but it is adjacent to an unresolved x-ray source (Ott et al. 2005a), as discussed below.

5. Discussion

5.1. Relation between Star Formation and Gas

As can be seen in Figure 17, the highest H I column density region roughly corresponds to the region of strongest Hα emission. This is seen in other BCDs as well (van Zee et al. 1998). There is diffuse Hα emission that spreads to the north, but not as far as the H I emission. Thuan et al. (2004) find that there is weak continuum emission (1.4 GHz) associated with the Hα emission; with a slight extension to the north at 1.4 GHz as well. Without a spectral index, they were unable to verify that the continuum emission is mainly thermal in nature (and thus directly due to to the H II region), but it does seem likely.

Ott et al. (2005a,b) presented *Chandra* x-ray observations of several dwarf starburst galaxies, including VII Zw 403. Their data show no diffuse x-ray emission associated with VII Zw 403. They found that the diffuse x-ray emission they detected in the other galaxies

in their sample was probably associated with the development of galactic winds from coronal gas heated by star formation. They suggest that the lack of detected diffuse x-ray emission for VII Zw 403 (they give an upper limit of 2.8×10^{38} erg s^{-1}) could be due to several possible factors, including low metallicity or smaller volume. The expanding Hα shells in the two galaxies with no detected diffuse x-ray emission (VII Zw 403 and I Zw 18) are 10-17 Myr older than those in the galaxies for which they do detect diffuse emission. Perhaps a coronal wind never developed, or perhaps it has already had time to cool.

Ott et al. (2005a) did detect one unresolved x-ray source whose power-law spectral index is consistent with that of an x-ray binary, but did not detect the filaments or lobes seen by Papaderos et al. (1994) from ROSAT data. Similar x-ray sources in the Ott et al. (2005a) sample of 8 starbursting galaxies are located near "bright H II regions, rims of superbubbles or young stellar clusters." The location of the unresolved x-ray source relative to the Hα emission can be seen in Figure 17. The x-ray source is located near, but not coincident with, an Hα knot. As seen in Figures 16 and 17, the x-ray source is also on the north edge of the high dispersion knot, and is located in/on the northeast side of the depression/cavity in the H I, in a smaller region of even lower density. Recall that the broadband surface photometry (Figure 6) was consistent with constant star formation in the outer regions over the past 10–20 Gyr, with more recent star formation (past 200 Myr) in the central regions. If the x-ray source is, indeed, an x-ray binary, then perhaps we are seeing an evolved stellar system located near a region of recent star formation, and also near a region of disturbed neutral gas. The logical explanation is that a star formation episode and/or resulting supernova has injected energy into the H I, increasing the dispersion; and depleting or perhaps clearing out some of the neutral gas.

To test this, we examined the kinematics of the gas in the B+C+D$_0$ cube in a small region around the x-ray source. To enhance the signal-to-noise in the spectra, we "collapsed" a six-pixel square region centered on the x-ray source to a single pixel, and then examined the resulting spectrum. There was a fairly clear double-peak visible, so we fit a pair of gaussians to them (using XGAUS in AIPS). The two peaks are separated by 13.5 km s^{-1}. This is consistent with expansion (or contraction) of ~ 7 km s^{-1}. The apparent radius of the depression around the x-ray source in the B+C+D$_0$ data is ~ 105 pc, which is roughly the same size as the beam. This means that the region may not be resolved, so this size is an upper limit. If we assume a constant expansion of 7 km s^{-1}, we get approximately 15 Myr to clear out a depression of that size.

We then tried to estimate the amount of energy required to form such a depression using the method in Chevalier (1974). Here we assume a spherically symmetric expansion. If the expansion has already blown out of the disk, this may not be the case (and would increase

the estimated age of the feature; see below). For a velocity of 7 km s^{-1} and a radius of 105 pc, we find the total energy required to be $E_s = 1.6 n_0^{1.12} \times 10^{51}$ ergs. To get an estimate for the density, n_0, we assumed a pre-existing column density of 1.5×10^{21} cm^{-2} based on the average density in the region around the small depression, and a scale height for the galaxy of 200 pc. The scale height was taken to be approximately equal to the radius of the larger H I depression/cavity (see below). This gives us $n_0 = 1.0$ cm^{-3}, and a resulting total energy of 1.6×10^{51} ergs. This is similar to the 10^{51} ergs from a typical Type II supernova, so it is feasible in this sense. We then attempted to apply the models of McCray & Kafatos (1987) for the formation of supershells from stellar winds and supernovae to estimate the number of stars with masses greater than $7 M_\odot$ required to produce a hole of a given size. The resulting number was approximately 200, of which about 50 should be O stars. However, the resulting timescale for shell formation calculated from the models was short, only 2 Myr. In this short time, the expansion due to the star formation is still primarily from stellar winds; and it is unlikely that any stars would yet have exploded as supernovae, and we should be able to see an OB association of this size—which we don't. So about all we can conclude is that the x-ray source appears to be coincident with an expanding depression in the H I; and adjacent to a region of disturbed gas to the south.

We also examined the kinematics of the gas around the edges of the larger depression/cavity in the H I. However, no expansion was detected. If we now use the average velocity dispersion in the gas (9 km s^{-1}) as an upper limit to any expansion, with a radius of 205 pc we obtain a lower limit of 22 Myr for a hole this size to form. Because we don't detect expansion, the hole could be stalled because it has broken out and is freely expanding perpendicular to the disk, and so could be older than that. We used the same methods to estimate the required energy and number of stars required to form such a depression as for the area around the x-ray source. This time, we used a column density of 2.5×10^{21} cm^{-2} based on the existing gas density around the cavity; giving us an n_0 of 1.6 cm^{-3}. The required energy is then 3×10^{52} ergs (equivalent to approximately 30 SNe). However, from the McCray & Kafatos (1987) equations, the estimated number of stars needed to create such a large depression via winds (and possibly supernovae, but see the timescale discussion, below) with masses greater than $7 M_\odot$ is then 2800, which is extremely high. If there were a young cluster that large, it would be easily visible. This suggests an older age for the formation of the large H I cavity; or perhaps the gas was slowly depleted/blown-out over long time-scales by a series of star-forming events rather than by one large cluster.

A more serious problem with applying the McCray & Kafatos (1987) model is that doing so results in a calculated timescale of only 3 Myr; which is not only short in stellar evolution terms, but also inconsistent with the lower limit of 22 Myr we calculated, above. A similar disconnect was found by Lynds et al. (1998) for formation of the large H II regions in VII Zw

403. They used the Wide Field Planetary Camera 2 (WFPC2) on the *Hubble Space Telescope* (HST) to produce color-magnitude diagrams (CMDs) of several of the bright H II regions in VII Zw 403. The brightest H II region (visible as the darkest region of the grayscale in Figure 17 and marked in Figure 18) was consistent with an OB association containing approximately 25 bright blue (O type) stars; the age of the cluster based on the CMD was 4–5 Myr. From their ground-based long-slit emission line spectra of the H II regions, they were able to detect expanding Hα shells; including a partial shell around the brightest H II region with a diameter of 79 pc and an expansion velocity of $\sim$ 65 km s^{-1}. They then attempted to use the McCray & Kafatos (1987) models as we did, but they also found a timescale that was too short: $\sim$ 1 Myr, which did not match the 4–5 Myr age estimate from the CMD. They concluded that perhaps this indicated that the starburst that formed the association was not instantaneous (Shull & Saken 1995).

Lynds et al. (1998) also produced CMDs of some of the central areas of VII Zw 403. The location of their "center" and "north" fields are marked in Figure 18, which shows the HST image with contours from the B+C+D$_{-1}$ integrated flux map. Neither field corresponds exactly with the H I cavity/depression, but the "north" field is located on the east side of it, and just south of the x-ray source. The CMD for the "north" field is less rich in massive stars than the one for the "center," which revealed approximately 20 red supergiants ($>$ 10 Myr) and some blue supergiants ($\sim$ 5 Myr), but both regions contain a mixed-age population of stars with ages of 5 and 10 Myr. In general, Lynds et al. (1998) find a relatively smooth elliptical distribution of the evolved stars with a stellar surface density that falls off exponentially. The younger, bluer massive stars tend to exhibit clustering into associations and groups, and are primarily located in the central regions of the galaxy. The youngest are associated with the bright H II regions, which we find are co-located with H I peaks (Figure 19). They posit star formation 1–2 Gyr ago followed by a strong starburst episode 600–800 Myr ago, with less vigorous star-formation since then. Interestingly, the kinematic center of VII Zw 403 as identified by the rotation curve analysis lies close to the center of the large H I cavity. If the cavity is the result of star-formation, this would be consistent with centrally-concentrated star-formation activity in the past. There is evidence that stellar feedback from star formation events can and does create sometimes large ($\approx$ 1 kpc) H I holes and shells, as found by Weisz et al. (2009) in IC 2574.

Another possibility for forming the hole is consumption of the gas by star formation. The timescale to consume the gas that filled the hole at the current star formation rate, given our estimate of the pre-existing level of the gas in that region, is of order 700 Myr. This is relatively short if star formation has been on-going in this region for that extended period of time. Alternatively, the original gas in this region could have been consumed quite quickly by the starburst that took place 600–800 Myr ago (Lynds et al. 1998), but we then

require that the hole not be replenished very rapidly, which seems unreasonable given that the hole should have filled in long ago just from the dispersion in the gas.

5.2. Origin of the Starburst

One possible explanation for the enhanced star formation episode that characterizes BCDs is proposed by Salzer et al. (1999), who suggest that it is a natural consequence of the central mass density concentration found in BCDs. In an optical study of a sample of 18 BCDs and 11 dIrrs, they find that when the luminosity contribution from the starburst is ignored (by fitting the underlying host galaxy's surface brightness profile as determined from an exponential fit to only the outer portions), the underlying hosts of BCDs have shorter scale lengths and higher central surface brightnesses than dIrrs with similar absolute magnitudes. They cite the shorter scale lengths as evidence of stellar compactness: that BCDs are low-surface brightness galaxies with the highest central stellar mass concentrations in the dwarf spectrum.

There is some evidence that this may be the case for the H I gas in BCDs as well: van Zee et al. (1998) plotted H I surface density profiles for a sample of BCDs and dIrrs, and found that the gas in BCDs is more centrally concentrated than in similar dIrrs. It is commonly thought that the gas surface density must exceed a critical threshold in order to support a starburst[6] (Kennicutt 1989); Salzer et al. (1999) also suggest that the high central mass density concentration allows these galaxies to retain their gas, allowing episodic bursts, and calculations by Mac Low & Ferrara (1990) indicate that mass loss should be minimal for galaxies with gas masses greater than 10^7 $M_\odot$. A follow-up study of the H I in a sample of BCDs by Salzer et al. (2002) found that the M_{HI}/L_B for these galaxies is about twice as high as that for low surface brightness dwarfs when only the luminosity of the underlying low-surface brightness component of the BCD is taken into account. This provides a significant gas reservoir to support the starburst episodes, and could enhance the ability of the galaxy to retain gas during/after a burst. Additionally, if the gas remains concentrated even after a burst, then the timescale between bursts could be short. This would make it difficult to find a BCD in the "off" state.

If this hypothesis is correct then we would expect VII Zw 403 to exhibit signs of central compactness, both optically and in the H I. We find that compared to the sample in

---

[6]Although azimuthal averages of the gas density in dwarfs rarely exceed this critical value, there is evidence that local values in the region of active star formation do (Hunter et al. 2001; van der Hulst et al. 1993; van Zee et al. 1997; Meurer et al. 1998; de Blok & Walter 2006).

Salzer et al. (1999), VII Zw 403 has a slightly lower μ_{B_0} at a given M_B than their sample of BCDs, although slightly higher than for their LSBDs. As mentioned in §3, VII Zw 403's scale length (relative to its M_V) lies at the peak of the distribution of the sample of dIms and BCDs plotted in Hunter & Elmegreen (2006). Compared to the Salzer et al. (1999) sample, however, it is large not only for their sample of BCDs, but also compared to their LSBD sample. So the underlying stellar component does not appear to be greatly centrally concentrated. However, there are some indications for central concentration in the H I on larger scales (i.e. at a linear resolution similar to that for which structure is seen in the H I in dIrrs; see Figure 9).

However, since the vigorous star formation episodes that characterize BCDs are relatively short-lived compared to the age of the host galaxy, perhaps these systems don't start out with a high central mass concentration. Van Zee et al. (2001) finds that BCDs are low angular momentum systems, and suggests that they have collapsed to more centrally concentrated systems with steeper rotation curves. This affects the critical threshold density for star formation, and makes BCDs more susceptible to star bursts than higher angular momentum systems. This "collapse" requires a redistribution of mass in the galaxy. One proposed mechanism for mass redistribution and angular momentum transfer in low mass BCDs (without nearby companions) is a barlike torque arising from the irregular symmetry and irregular mass distribution in these small systems, or from an elongated dark matter halo (Hunter & Elmegreen 2004). Such mass flow should show up in the rotation pattern of the gas disk as a central twisting of the isovelocity contours. VII Zw 403 has a change of 15–20° between the NE and SW parts of the galaxy, so we can't rule out the possibility of some kind of mass flow in the gas disk.

Another possible mechanism for flattening the gravitational potential and expansion of the stellar component is suggested by Papaderos et al. (1996b), who propose that the heating of the ISM by the energy from the starburst could be the mechanism for mass and angular momentum redistribution. Although VII Zw 403's scale length is not particularly short, which could indicate that it has undergone some expansion, the lack of diffuse x-ray as well as the lack of extensive large-scale structure in the H I (the H I depression discussed above occupies only a small, central part of the galaxy) would seem to indicate that not much energy has been injected into the galaxy as a whole by star formation. It seems unlikely, then, that enough energy would have been produced to initiate any significant redistribution of the mass in the galaxy, especially the stellar component. In conclusion, it isn't clear that this theory of large-scale mass re-arrangement can explain what we see in VII Zw 403.

Interactions, either with other galaxies or with small gas companions, have also been proposed as the triggering mechanism for the starbursts that occur in BCDs (see Brosch et al.

2004 for an overview of the literature), yet surveys to detect nearby possible perturbers around BCDs have had mixed results (e.g. Campos-Aguilar & Moles 1991; Telles & Terlevich 1995; Taylor 1997; Putman et al. 1998; Telles & Maddox 2000; Pustilnik et al. 2001, 2003; Brosch et al. 2004; Hunter & Elmegreen 2004), VII Zw 403 would seem to be in the set of galaxies that haven't been tidally triggered, as we have found no nearby H I clouds or companion galaxies. However, if it had accreted a small perturber in the distant past, this might be difficult to detect.

There is observational evidence that some dwarf systems have undergone accretion or merger events in the past. A nearby example is thought to be IC 10, which Wilcots & Miller (1998) argue still has primordial gas settling into the galaxy via accretion. Classic signatures of accretion include the appearance of two distinctly different kinematic components, visible in the H I or stellar velocity fields. Although the gas isovelocity contours for VII Zw 403 are somewhat perturbed, this isn't unusual for BCDs (§4.3), and there don't appear to be two completely separate components despite the change in position angle of the H I kinematic axis. Another accretion signature is a misalignment between the optical and H I axes. Hunter & Wilcots (2002) plotted the difference between optical and H I kinematic axes for 47 Im and Sm galaxies taken from Swaters (1999) and found that about half had offsets less than $10°$, with the maximum being $40°$. For VII Zw 403, the optical axis is at $-11°$. In the NE half of the galaxy, the H I kinematical axis is at $+45°$ to $+50°$, and is around $+20°$ to $+30°$ in the SW part, so there is a somewhat significant misalignment between the gas and optical components of between $30°$ and $60°$.

For further comparison, we look to the gas-rich Im galaxy DDO 26, for which Hunter & Wilcots (2002) conclude that the most likely explanation for the lack of relaxation they detect in its gas kinematics is the on-going merger of two small gas-rich objects. They find an optical/H I axis misalignment of $60°$, along with a change in the H I position angle with radius. They also find that the velocity field of DDO 26 is fairly regular in the inner regions and becomes less so in the outer disk. These are features that are similar to but more extreme than those we see in VII Zw 403. Differences include the presence of a faint H I arm in DDO 26 and the detection of two separate peaks in the H I intensity which were both fairly broad (~ 40 km s^{-1}) in velocity. Additionally, DDO 26 is currently quiescent, with a SFR of 0.0004 $M_\odot$ yr^{-1} kpc^{-2} compared to VII Zw 403's rate of 0.02 $M_\odot$ yr^{-1} kpc^{-2}. So from these comparisons, it seems possible that VII Zw 403 underwent an accretion or merger event in the past.

Another possibility to explain the skew in the H I kinematic axis is that expansion of the H II regions has caused a subsequent expansion in the surrounding H I, lifting it out of the plane of the galaxy. If the near side of the galaxy is to the west (right), and we envision the expanding H I as distributed in a torus aligned with the plane of the galaxy, then gas

to the left of the kinematic center would be blue-shifted relative to the bulk of the galaxy. Likewise, the gas to the right of center would be somewhat behind the bulk of the galaxy and red-shifted. The expanding gas would then skew the observed velocity field in the sense that we see: the isovelocity contours in the north part will be skewed to the left, and those in the south skewed to the right. If the expansion is on the order of the 7 km s^{-1} we measured for the lowest density region around the x-ray source, or the 9 km s^{-1} limit set by the average dispersion, then in this slowly rotating galaxy, the expected skew would be large, which is what we see. In this case, the hole in the H I would be due to a combination of consumption and slow blow-out.

6. Summary

We have used multi-wavelength data to examine the relation between the stars and gas in VII Zw 403 in an effort to understand the origin of the starbursting activity that characterizes BCD galaxies. As for many BCDs, in the optical V-band we find a mostly symmetrical, elliptical distribution of stars; this is overlaid with a color gradient that is bluer in the central regions and redder in the outer. This indicates that the central regions have undergone star formation in the past 200 Myr, whereas the outer region colors indicate constant star formation over the past 10–20 Gyr. The galaxy also has a few large H II regions concentrated toward the center of the galaxy (within the inner 1.3 kpc) where star formation has occurred in the past 10 Myr. Most of the activity is in a large complex just south of the central part of the galaxy. Overall, the SFR for VII Zw 403 is at the high end of the normal range for dIrrs, which is, again, typical for BCDs. However, the galaxy can continue to form stars at this rate for at least 5 Gyr more; 10 Gyr if we include gas recycling (Brinchmann et al. 2004).

Our new VLA data in combination with earlier data resulted in a lower total H I flux detection than single-dish estimates; we believe this is due to inclusion of Milky Way emission in the single-dish spectra and in the low-resolution VLA observations. We have attempted to remove this Galactic contamination from our low-resolution (D configuration) data for our analysis here. Our total H I mass estimate then is 5×10^7 $M_\odot$, which is lower than the median for the Salzer BCD sample (Salzer et al. 2002), but within the normal range of values. However, the M_{HI}/L_B indicates that VII Zw 403 is somewhat gas-rich for a BCD of similar luminosity. Conversely, it may be "luminosity-poor" relative to other similarly-sized BCDs: earlier work by Lynds et al. (1998) concluded that the SFR for VII Zw 403 was up to 30 times greater 600–800 Myr ago. Perhaps we are seeing it post-burst. The idea that VII Zw 403 is presently past the peak of a starburst event could also explain the non-detection

of diffuse x-ray emission by Ott et al. (2005a,b), indicating a lack of coronal wind or that it has had time to cool.

The H I velocity field, although complex with a change in position angle of the kinematic axis between the NE and SW components of about 15–20°, is not that unusual for a BCD. We see no other strong indications of a large-scale gravitational interaction in the velocity field, such as tidal tails or strewn-about H I. The skew in the velocity field can, however, be explained if the H I in the galaxy is undergoing a general symmetric expansion away from the plane on both sides surrounding the star-forming region as a result of pressure from the Hα region. The rotation curve is essentially solid-body for both halves of the galaxy, and with correction for asymmetric drift, produces a dynamical mass estimate that is similar to those of other BCDs (Taylor et al. 1994; van Zee et al. 1998, 2001).

If the galaxy is post-starburst, then one might expect to see some effect in the interstellar medium from the energy injected by stellar winds and supernovae. Additionally, star formation should use up some of the neutral gas in the galaxy. In accordance with this, although the H I is more centrally concentrated in VII Zw 403 than in dIrrs, the central H I surface density is lower than is typical for the BCDs in the van Zee et al. (1998) sample, and the H I is more extended—out to 4.3 R_{25} (2.3 R_H). At large scales (650 pc), the H I distribution appears relatively smooth as for most BCDs. This is in contrast to dIrr galaxies, which at the same scale often show structure in the gas component in the form of holes, shells, and ridges. For VII Zw 403 however, we begin to see some structure in the H I distribution only at small (200 pc) scales.

There is clearly a connection between recent star formation and the H I distribution and kinematics in the galaxy. The youngest stars (4–5 Myr old) are located near H II regions and local peaks in the H I, with the regions of highest H I column density corresponding to the regions of strongest Hα flux (as seen in other BCDs). Our H I maps also show that the regions of higher dispersion are located near, although not completely coincident with, with Hα regions; perhaps in response to the energy injected by the star formation activity. Interestingly, the region of highest dispersion in our map is directly adjacent to the unresolved x-ray source detected by Ott et al. (2005a) that could be an x-ray binary. The source is located near an H II region, and is in a small lower-density region at the edge of a larger depression or cavity in the H I. The center of the large H I cavity is coincident with the kinematic center of the H I velocity field.

We attempted to investigate whether the small low-density region could be the result of star formation/SNe blowing a hole in the gas. Although both the amount of energy required and the number of massive stars needed were reasonable, the timescale from the shell formation model was too short for many SNe to have already occurred. We performed

the same analysis for the (stalled) large cavity in the H I, but found that in addition to requiring the presence of a large star cluster (not seen), the timescale from the model was again too short. Similar timescale discrepancies were found by Lynds et al. (1998), leading them to invoke non-instantaneous starburst/star-formation activity in a series of events.

So we are brought back to the question of what triggered the vigorous star formation episode that apparently peaked in the past but is still ongoing today. We have investigated three possible triggers: tidal forces from an external perturber, inherent central mass density concentration, and accretion of a smaller object. We found no nearby large or small perturbers, so it has apparently not been tidally triggered. VII Zw 403's mass doesn't appear to be strongly centrally concentrated either, as evidenced by its optical scale length, lower central surface brightness, and lower H I surface density than comparable BCDs. This leaves us with an accretion event. There is evidence for accretion in some dwarf systems, including some Local Group dwarfs. Compared to another suspected accretion/merger system (DDO 26), VII Zw 403 has some similarities but less extreme signatures. Of the three possible triggers we have investigated, this seems the most likely; although the evidence is far from conclusive.

Facilities: VLA GALEX Lowell Observatory

Table 1.   VLA Observations

Parameter	D configuration	C configuration	B configuration
Observation Date	1997 Nov. 10	1992 April 11	2006 Sept. 10
Time on Source (min)	253	220	546
Central Velocity (km s^{-1})	-60	-60	-60[a]
Bandwidth (MHz)	1.56	1.56	1.56
No. of Channels	128	128	128
Velocity Resolution (km s^{-1})	2.6	2.6	2.6
Beam Size (arcsec)	72.91×53.57	$\cdots$	$\cdots$
Single Channel r.m.s. (mJy beam^{-1})	0.93	$\cdots$	$\cdots$
Single Channel r.m.s. (K)	0.28	$\cdots$	$\cdots$

[b]Doppler tracking not available; central fixed frequency chosen to correspond to -60 km s^{-1}. See text for details.

[a]Natural weighting

Table 2.   Combined Configuration Parameters

Parameter	C+D$_1$	B+C+D$_1$	B+C+D$_0$	B+C+D$_{-1}$
Robustness Factor	+1	+1	0	−1
Beam Size (arcsec)	34.10×27.60	12.85×11.71	9.23×7.57	4.95×4.63
Beam Size (pc)	730×590	280×250	200×210	110×990
Single Channel r.m.s. (mJy beam^{-1})	0.83	0.80	0.86	0.90

Table 3. Summary of Properties.

Parameter	Value
R.A. (B1950; V)	$11^{\rm h}\ 24^{\rm m}\ 33\overset{\rm s}{.}4\ \pm 4''$
Decl. (B1950; V)	$79°\ 16'\ 10'' \pm\ 3''$
R.A. (B1950; H I)	$11^{\rm h}\ 24^{\rm m}\ 35\overset{\rm s}{.}1 \pm\ 10\overset{\rm s}{.}3$
Decl. (B1950; H I)	$79°\ 16'\ 18'' \pm\ 27''$
b/a (V)	0.49
P.A. (V)	$-11°$
D (Mpc)	4.4
$M_{\rm HI}$ ($M_\odot$)	5.23×10^7
$R_{\rm HI}$[a] (arcsec, kpc)	157, 3.35
$E(B-V)_f$[b]	0.023
R_{25} (arcsec, kpc)	36.5, 0.78
R_H (arcsec, kpc)	68.95, 1.47
μ_0^V (magnitudes arcsec^{-2}) .	23.12 ± 0.09
R_D^V (kpc)	0.50 ± 0.01
M_{V_0} (magnitudes)	-14.26 ± 0.009
$(U-B)_0$	-0.50 ± 0.01
$(B-V)_0$	0.27 ± 0.01
$(V-J)_0$	1.30 ± 0.01
(FUV−NUV)$_0$	0.17 ± 0.01
(NUV−V)$_0$[c]	0.70 ± 0.01
$\log L_{H\alpha,0}$ (ergs s^{-1})	39.34 ± 0.001
$\log L_{NUV,0}$ (ergs s^{-1} Hz^{-1})	26.07 ± 0.001
SFR$_{H\alpha}$[d] ($M_\odot$ yr^{-1})	0.015
SFR$_{FUV}$[d] ($M_\odot$ yr^{-1})	0.013
SFR$_{\rm D,H\alpha}$[e] ($M_\odot$ yr^{-1} kpc^{-2})	-1.72

[a]Measured to $N_{\rm HI} = 1 \times 10^{19}$ cm^{-2}.

[b]$E(B-V)_f$ is foreground reddening due to the Milky Way (Burstein & Heiles 1984). For the stars

in VII Zw 403, we assume an additional internal reddening of 0.05 magnitude; for the H II regions we assume an additional internal reddening of 0.1 magnitude.

[c]NUV is an AB magnitude.

[d]Star formation rates derived from $L_{H\alpha}$ or the ultraviolet using the formulae of Hunter et al. (2010) that integrates from 0.1 $M_\odot$ to 100 $M_\odot$ with a Salpeter (1955) stellar initial mass function.

[e]Star formation rate normalized to the area within one scale-length R_D^V.

REFERENCES

Begum, A., & Chengalur, J. N. 2004, A&A, 413, 525

Bell, E. F., & de Jong, R. S. 2001, ApJ, 550, 212

Brandt, J. C. 1960, ApJ, 131, 293

Bravo-Alfaro, H., Brinks, E., Baker, A. J., Walter, F., & Kunth, D. 2004, AJ, 127, 264

Brinchmann, J., Charlot, S., White, S. D. M., Tremonti, C., Kauffmann, G., Heckman, T., & Brinkmann, J. 2004, MNRAS, 351, 1151

Brosch, N., Almoznino, E., & Heller, A. B. 2004, MNRAS, 349, 357

Bruzual, G., & Charlot, S. 2003, MNRAS, 344, 1000

Burstein, D., & Heiles, C. 1984, ApJS, 54, 33

Cairós, L. M., Caon, N., Papaderos, P., Noeske, K., Vílchez, J. M., García Lorenzo, B., & Muñoz-Tuñón, C. 2003, ApJ, 593, 312

Campos-Aguilar, A., & Moles, M. 1991, A&A, 241, 358

Cardelli, J. A., Clayton, G. C., & Mathis, J. S. 1989, ApJ, 345, 245

Carignan, C., & Beaulieu, S. 1989, ApJ, 347, 760

Carignan, C., Beaulieu, S., & Freeman, K. C. 1990, AJ, 99, 178

Chevalier, R. A. 1974, ApJ, 188, 501

Coleman, M., Da Costa, G. S., Bland-Hawthorn, J., Martínez-Delgado, D., Freeman, K. C., & Malin, D. 2004, AJ, 127, 832

Côté, S., Carignan, C., & Freeman, K. C. 2000, AJ, 120, 3027

Condon, J. J., Cotton, W. D., Greisen, E. W., Yin, Q. F., Perley, R. A., Taylor, G. B., & Broderick, J. J. 1998, AJ, 115, 1693

de Blok, W. J. G., & Walter, F. 2006, AJ, 131, 363

de Vaucouleurs, G., de Vaucouleurs, A., Corwin, H., Buta, R., Paturel, G., & Fouqué, P. 1991, Third Reference Catalogue of Bright Galaxies (New York, Springer-Verlag)

DePoy, D. L., Atwood, B., Byard, P. L., Frogel, J., & O'Brien, T. P. 1993, SPIE, 1946, 667

Fazio, G. G., et al. 2004, ApJS, 154, 10

Hodge, P. W., & Hitchcock, J. L. 1966, PASP, 78, 79

Huchtmeier, W. K., & Richter, O.-G. 1986, A&AS, 63, 323

Huchtmeier, W. K. & Richter, O.-G. 1989, A General Catalog of H I Observations of Galaxies. The Reference Catalog, XIX (New York: Springer-Verlag)

Hunter, D. A. 1997, PASP, 109, 937

Hunter, D. A., & Elmegreen, B. G. 2004, AJ, 128, 2170

Hunter, D. A., & Elmegreen, B. G. 2006, ApJS, 162, 49

Hunter, D. A., Elmegreen, B. G., & Ludka, B. C. 2010, AJ, 139, 447

Hunter, D. A., Elmegreen, B. G., & Martin, E. 2006, AJ, 132, 801

Hunter, D. A., Elmegreen, B. G., & van Woerden, H. 2001, ApJ, 556, 773

Hunter, D. A., & Hoffman, L., 1999, AJ, 117, 2789

Hunter, D. A., & Wilcots, E. M. 2002, AJ, 123, 2449

Izotov, Y. I., & Thuan, T. X. 1999, ApJ, 511, 639

Karachentsev, I. D., et al. 2002, A&A, 383, 125

Kennicutt, R. C. 1989, ApJ, 344, 685

Kennicutt, R. C., Balick, B., & Heckman, T. 1980, PASP, 92, 134

Landolt, A. U. 1992, AJ, 104, 340

Larson, R., & Tinsley, B. 1978, ApJ, 219, 46

Loose, H.-H., & Thuan, T. X. 1985, in Star-Forming Dwarf Galaxies and Related Objects, eds. D. Kunth, T. X. Thuan, & J. T. T. Van (Gif-sur Yvette: Ed. Frontiéres), 73

Lynds, R., Tolstoy, E., O'Neil, E. J., & Hunter, D. A. 1998, AJ, 116, 146

Mac Low, M.-.M, & Ferrara, A. 1999, ApJ, 513, 142

Martin, C. L. 1998, ApJ, 506, 222

Martin, D. C., et al. 2005, ApJ, 619, L1

McCray, R., & Kafatos, M. 1987, ApJ, 317, 190

Meurer, G. R., Freeman, K. C., & Dopita, M. A. 1992, AJ, 103, 60

Meurer, G. R., Staveley-Smith, L., & Killeen, N. E. B. 1998, MNRAS, 300, 705

Noeske, K. G., Papaderos, P., Cairòs, L. M., & Fricke, K. J. 2003, A&A, 410, 481

Oke, J. B. 1974, ApJS, 27, 21

Östlin, G., Amram, P., Bergvall, N., Masegosa, J., Boulesteix, J., & Márquez, I. 2001, A&A, 374, 800

Ott, J., Walter, F., Brinks, E., Van Dyk, S. D., Dirsch, B., & Klein, U. 2001, AJ, 122, 3070

Ott, J., Walter, F., Brinks, E. 2005a, MNRAS, 358, 1423

Ott, J., Walter, F., Brinks, E. 2005b, MNRAS, 358, 1453

Papaderos, P., Fricke, K. J., Thuan, T. X., & Loose, H.-H. 1994, A&A, 291, L13

Papaderos, P., Loose, H.-H., Fricke, K. J., & Thuan, T. X. 1996a, A&A, 314, 59

Papaderos, P., Loose, H.-H., Thuan, T. X., & Fricke, K. J. 1996b, A&AS, 120, 207

Puche, D., Westpfahl, D., Brinks, E., Roy, J.-R. 1992, AJ, 103, 1841

Pustilnik, S. A., Kniazev, A. Y., Lipovetsky, V. A., & Ugryumov, A. V. 2001, A&A, 373, 24

Pustilnik, S. A., Kniazev, A. Y., Pramskij, A. G., Ugryumov, A. V. & Masegosa, J. 2003, A&A, 409, 917

Putman, M. E., Bureau, M., Mould, J. R., Staveley-Smith, L., & Freeman K. C. 1998, AJ, 115, 2345

Sage, L. J., Salzer, J. J., Loose, H.-H., & Henkel 1992, A&A, 265, 19

Salpeter, E. E. 1955, ApJ, 121, 161

Salzer, J. J., & Norton, S. A. 1999, in IAU Colloq. 171, The Low Surface Brightness Universe, ed. J. I. Davies, C. Impey, & S. Phillipps (ASP Conf. Ser. 170) (San Franscisco: ASP), 253

Salzer, J. J., Rosenberg, J. L., Weisstein, E. W., Mazzarella, J. M., & Bothun, G. D. 2002, AJ, 124, 191

Schlegel, D. J., Finkbeiner, D. P., & Davis, M. 1998, ApJ, 500, 525

Schulte-Ladbeck, R. E., Hopp, U., Crone, M. M., & Greggio, L. 1999, ApJ, 525, 709

Searle, L., & Sargent, W. L. W. 1972, ApJ, 173, 25

Shull, J. M., & Saken, J. M. 1995, ApJ, 444, 663

Simpson, C. E., & Gottesman, S. T. 2000, AJ, 120, 2975

Simpson, C. E., Hunter, D. A., & Knezek, P. 2005a, AJ, 129, 160

Simpson, C. E., Hunter, D. A., & Nordgren, T. E. 2005b, AJ, 130, 1049

Skrutskie, M. F., et al. 2006, AJ, 131, 1163

Stewart, S. G., et al. 2000, ApJ, 529, 201

Stil, J. M., & Israel, F. P. 2002a, A&A, 389, 29

Stil, J. M., & Israel, F. P. 2002b, A&A, 392, 473

Stone, R. P. S. 1977, ApJ, 218, 767

Swaters, R. 1999, Ph.D. thesis, Rijksuniversiteit Groningen

Sung, E.-C., Han, C., Ryder, B. S., Chun, M.-S., & Kim, H.-I. 1998, ApJ, 499, 140

Taylor, C. L. 1997, ApJ, 480, 524

Taylor, C. L., Brinks, E., Pogge, R. W., & Skillman, E. D. 1994, AJ, 107, 971

Taylor, C. L., Brinks, E., Grahuis, R. M., & Skillman, E. D. 1995, ApJS, 99, 427

Taylor, C. L., Kobulnicky, H. A., & Skillman, E. D. 1998, AJ, 116, 2746

Telles, E., & Terlevich, R. 1995, MNRAS, 275, 1

Telles, E., & Maddox, S. 2000, MNRAS, 311, 307

Thuan, T. X., & Martin, G. E. 1981, ApJ, 247, 823

Thuan, T. X., Hibbard, J. E., & Lévrier, F. 2004, AJ, 128, 617

Thuan, T. X., Williams, T. B., & Malumuth, E. 1987, in Starburst and Galaxy Evolution, eds. T. X. Thuan, T. Montmerle, & J. T. T. Van (Gif-sur Yvette: Ed. Frontiéres), 151

Toomre, A. 1964, ApJ, 139, 1217

Tully, R. B., Boesgaard, A. M., Dyck, H. M., & Schempp, W. V. 1981, ApJ, 246, 38

van der Hulst, J. M., Skillman, E. D., Smith, T. R., Bothun, G. D., McGaugh, S. S., & de Blok, W. J. G. 1993, AJ, 106, 548

van den Bergh, S. 1988, PASP, 100, 344

van Zee, L., Haynes, M. P., Salzer, J. J., & Broeils, A. H. 1997, AJ, 113, 1618

van Zee, L., Skillman, E. D., & Salzer, J. J. 1998, AJ, 116, 1186

van Zee, L., Salzer, J. J., & Skillman, E. D. 2001, AJ, 122, 121

Walter, F., & Brinks, E. 1999, AJ, 118, 273

Weisz, D. R., Skillman, E. D., Cannon, J. M., Walter, F., Brinks, E., Ott, J., Dolphin, A. E. 2009, ApJ, 691, L59

Wilcots, E. M., & Hunter, D. A., 2002, AJ, 123, 1476

Wilcots, E. M., & Miller, B. W. 1998, AJ, 116, 2363

Wyder, T. K., et al. 2007, ApJS, 173, 293

Young, L. M., & Lo, K. Y. 1996, ApJ, 462, 203

Young, L. M., van Zee, L., Lo, K. Y., Dohm-Palmer, R. C., & Beierle, M. E. 2003, ApJ, 592, 111 %

Zwicky, F. 1964, ApJ, 140, 1467
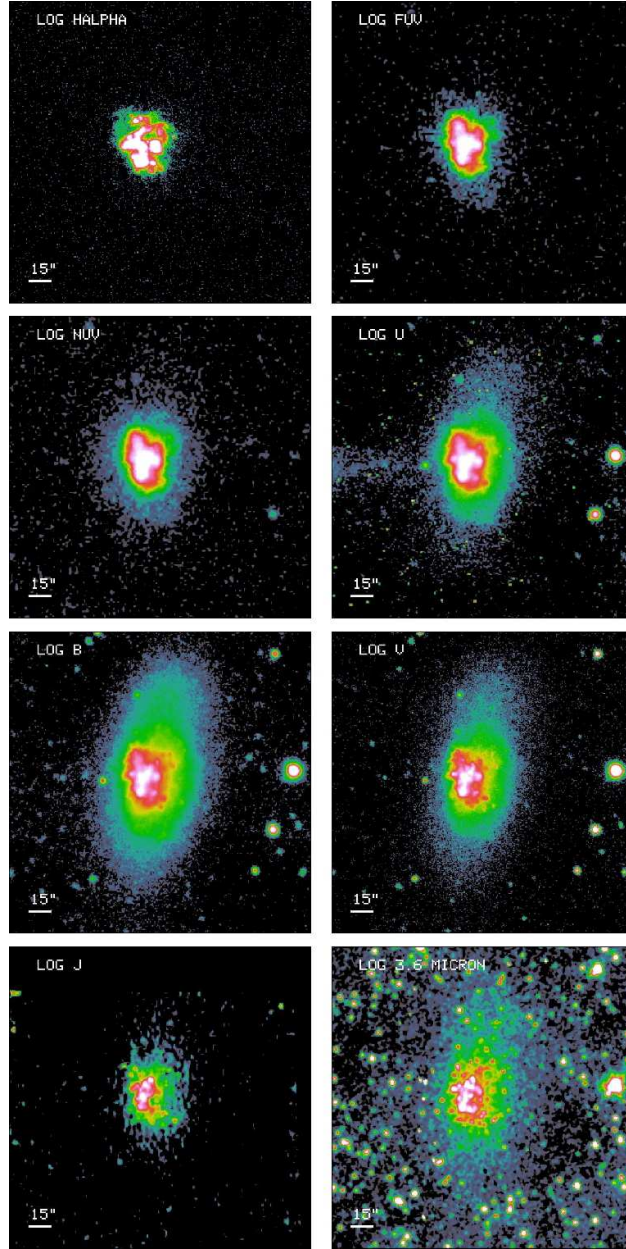
Fig. 1.— Images of VII Zw 403 in various passbands. The images are shown as the logarithm in order to allow the inner and outer structure to be viewed simultaneously. The images are also geometrically transformed to match the scale and orientation of the V image, and the same field of view is shown in each plot. North is up and East to the left.
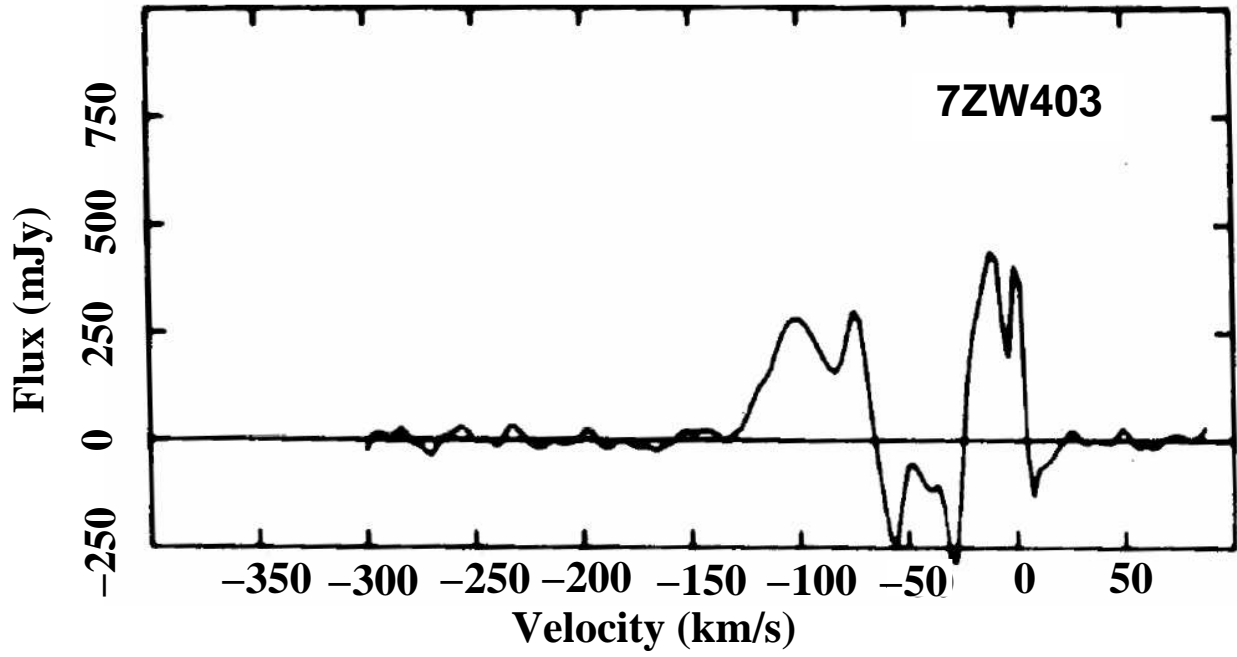
Fig. 2.— Single-dish spectrum from Thuan & Martin (1981).
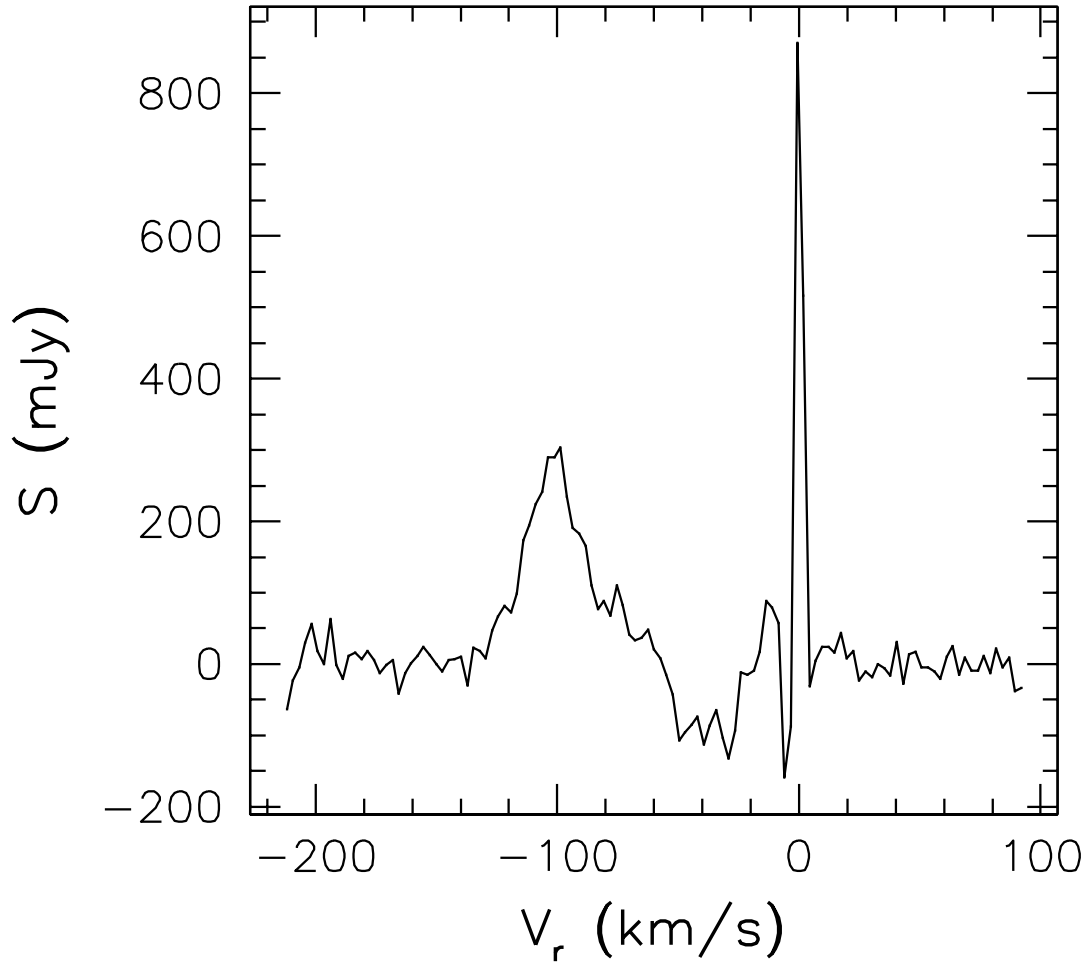
Fig. 3.— Summed flux in each channel from the uniformly-weighted D configuration data. The strong spike and absorption features near 0 km s^{-1}, as well as some of the emission from approximately -55 to -80 km s^{-1} are due to Galactic H I.
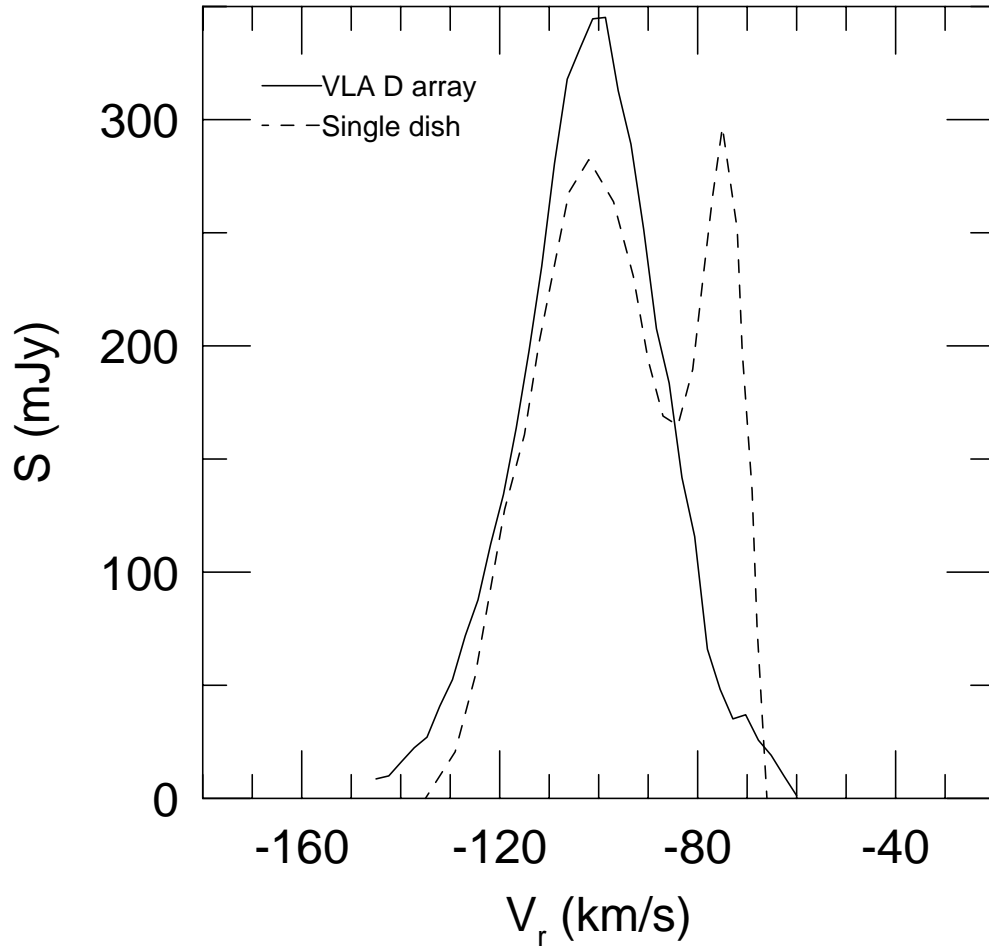
Fig. 4.— Summed flux in each channel from the naturally-weighted D configuration data (solid line) is plotted along with the single-dish detection by Thuan & Martin (1981) (dotted line). The emission located around -70 km s^{-1} is foreground H I from the Milky Way.
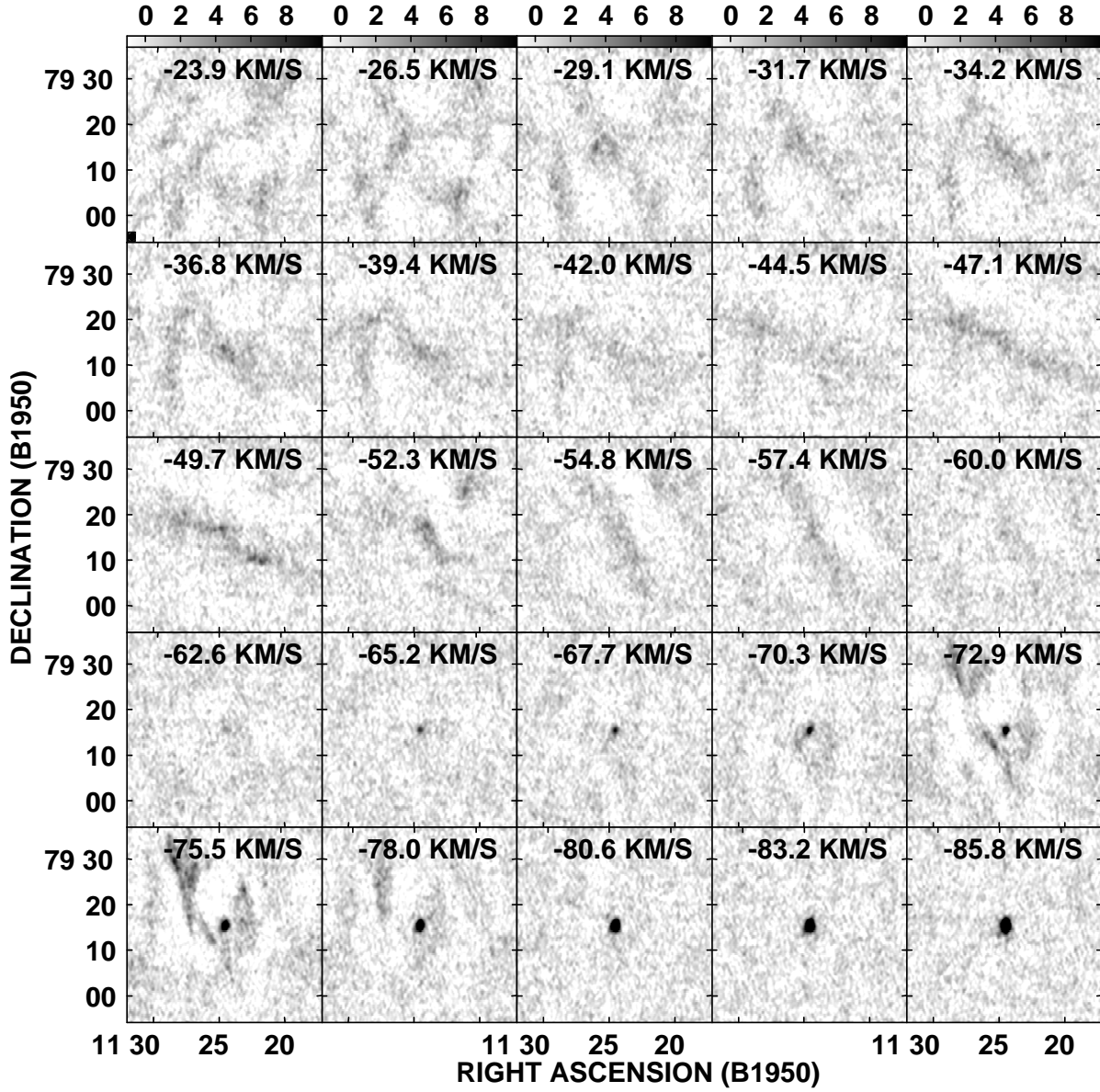
Fig. 5.— Channel maps from part of the D configuration data cube. Contaminating emission from the Milky Way is visible in the velocity range from -23.9 to -80.6 km s^{-1}. The strong concentrated emission in the center of the field is from VII Zw 403.
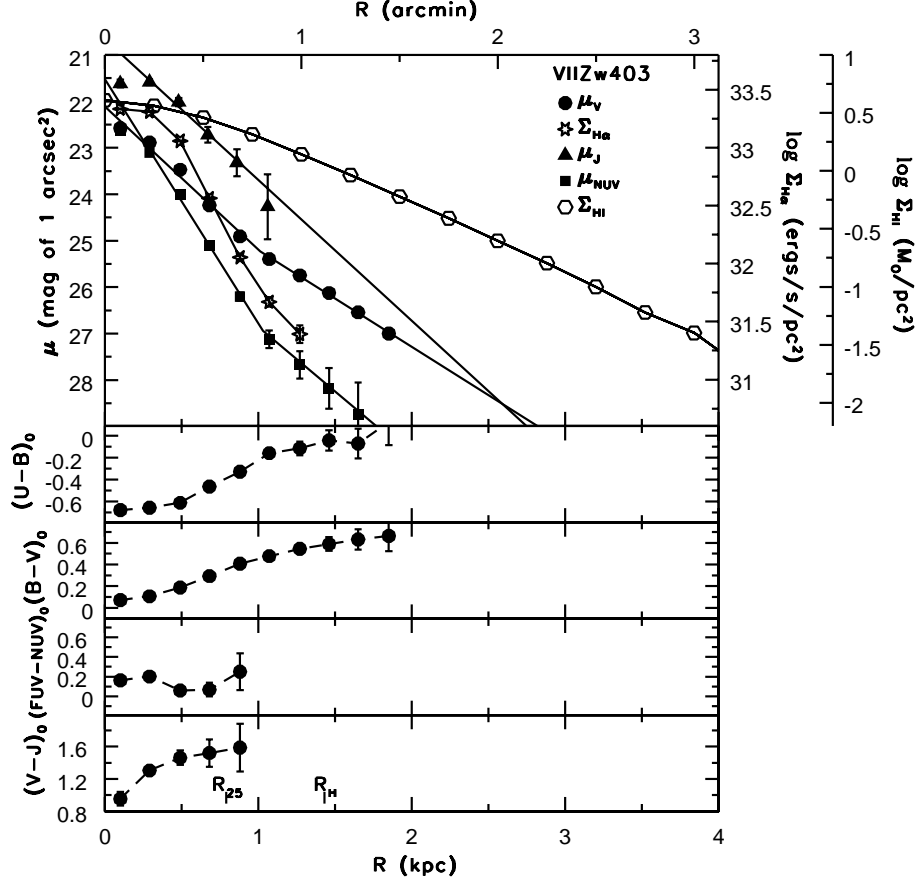
Fig. 6.— Azimuthally-averaged V, Hα, NUV, 3.6 μm, $(U-B)_0$, $(B-V)_0$, $(FUV-NUV)_0$, and $(V-J)_0$ surface photometry and H I surface density of VII Zw 403, using the V-band morphological center of the galaxy. The $UBVJ$ and NUV photometry are corrected for reddening as described in the text. The exponential fits to the V, 3.6 μm, and NUV-band surface brightness profiles are shown as solid lines in the top panel. These profiles are fit with two exponentials; the outer one shallower than the inner. The Hα luminosity is proportional to the star formation rate. The scales for $\Sigma_{H\alpha}$ and for Σ_{HI} have been set to cover the same logarithmic interval as the broad-band surface photometry covers in magnitudes and are shown on the right y-axis.
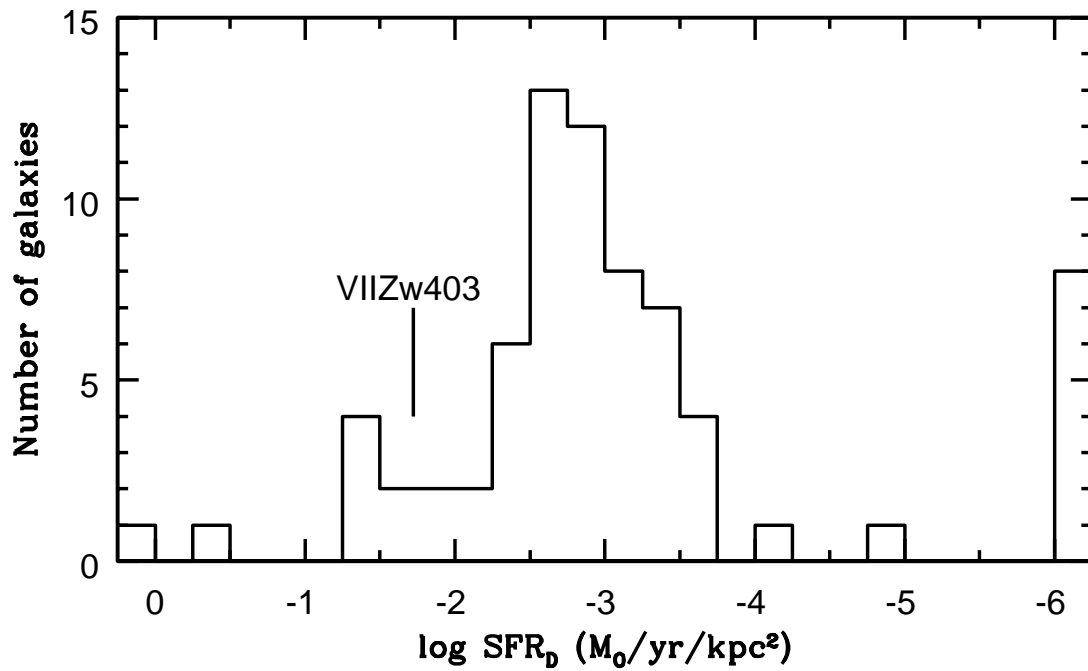
Fig. 7.— Star formation rate per unit area (SFR$_D$; from Hunter & Elmegreen (2004) for unbarred dIm galaxies. After Figure 11 from Hunter & Elmegreen (2006). SFR$_D$ is the integrated Hα-based star formation rate divided by the area in one V-band disk scale length of the galaxy. VII Zw 403 has a star formation rate that is significantly higher than the median in this sample.
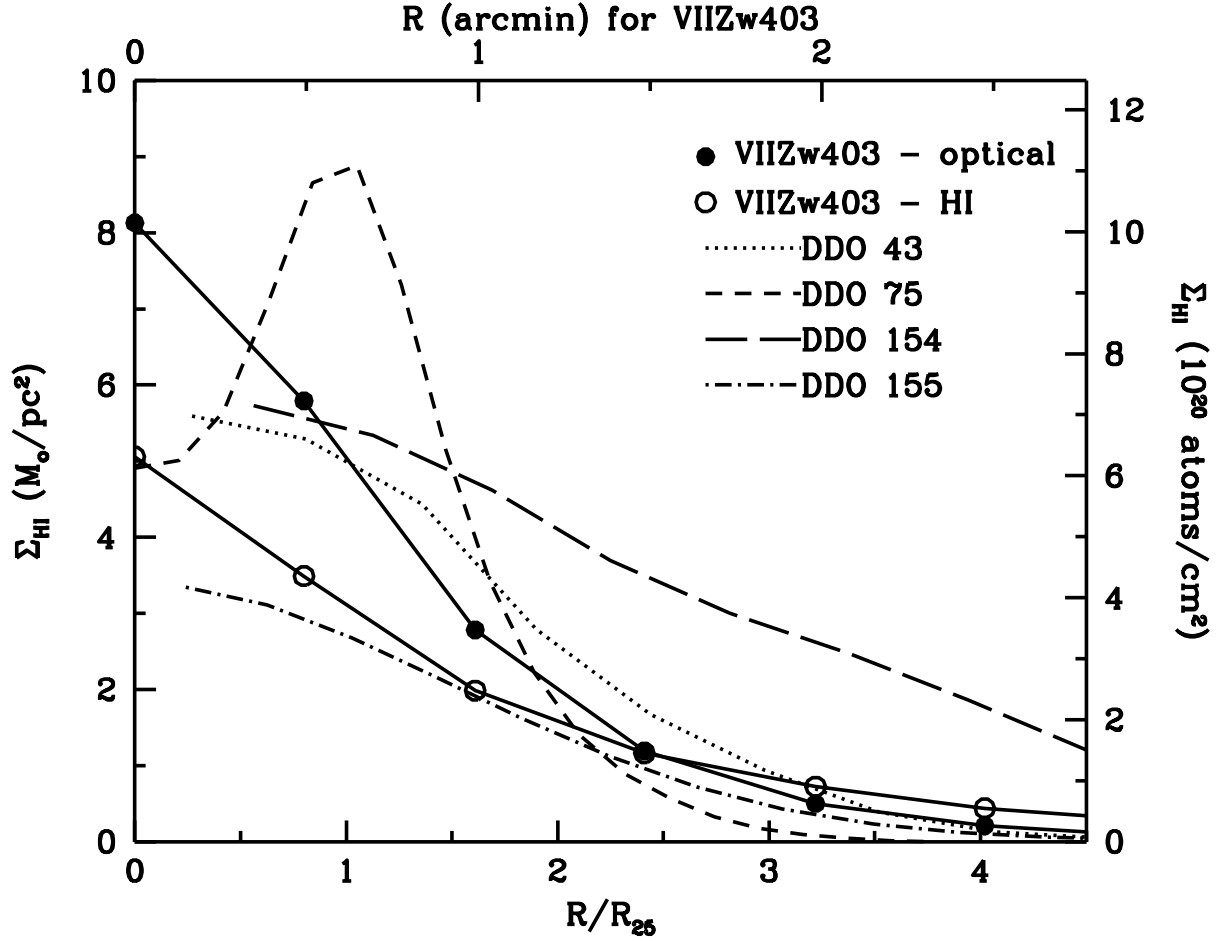
Fig. 8.— H I surface density in VII Zw 403 from the $C+D_1$ data. The line with the solid circles labelled "optical" used the center, inclination (66°), and position angle (−11°) from the V-band data. The line with open circles labelled "H I" used the center, inclination (77°), and average position angle (47°) from the H I rotation curve for the NE half of the galaxy. H I surface density profiles for galaxies with similar beam/$R_{1/2}$ or beam/R_{25} ratios are also shown. Data for these profiles are from DDO 43 (Simpson et al. 2005b); DDO 75 (Sextans A) (Wilcots & Hunter 2002); DDO 154 (Carignan & Beaulieu 1989); and DDO 155 (Carignan et al. 1990).
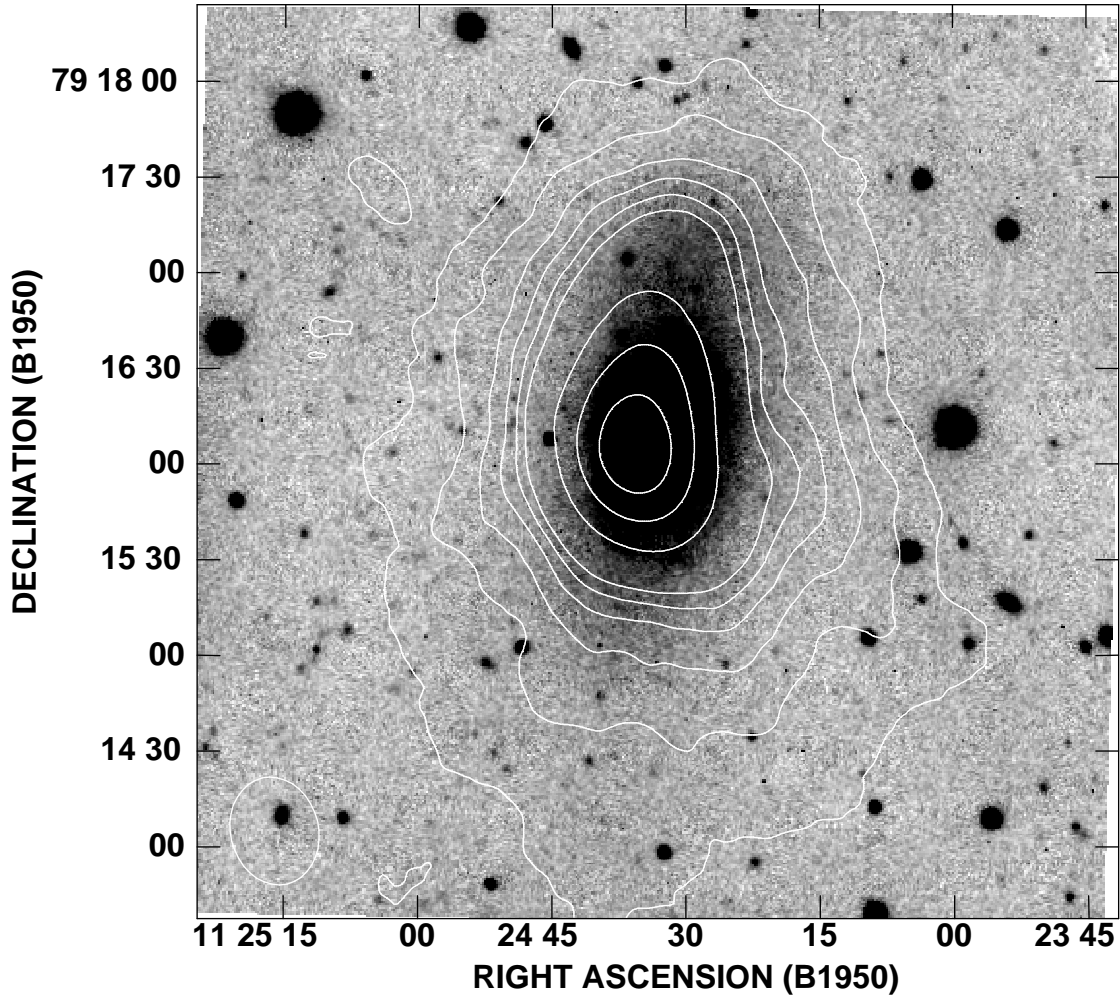
Fig. 9.— The V image overlaid with contours from the C+D$_1$ configuration integrated flux map. The beam size is indicated in the lower left corner. The levels are (2, 10, 20, 30, 40, 50, 100, 150, and 200) $\times 10^{19}$ cm^{-2}. The lowest contour is at 1.3σ. (A single-channel 2σ detection integrated over 3 channels is equivalent to a column density of 1.5 $\times 10^{19}$ cm^{-2}, which we take as indicative of the noise level in the integrated map.) The field of view is approximately 5′$\times$ 5′.
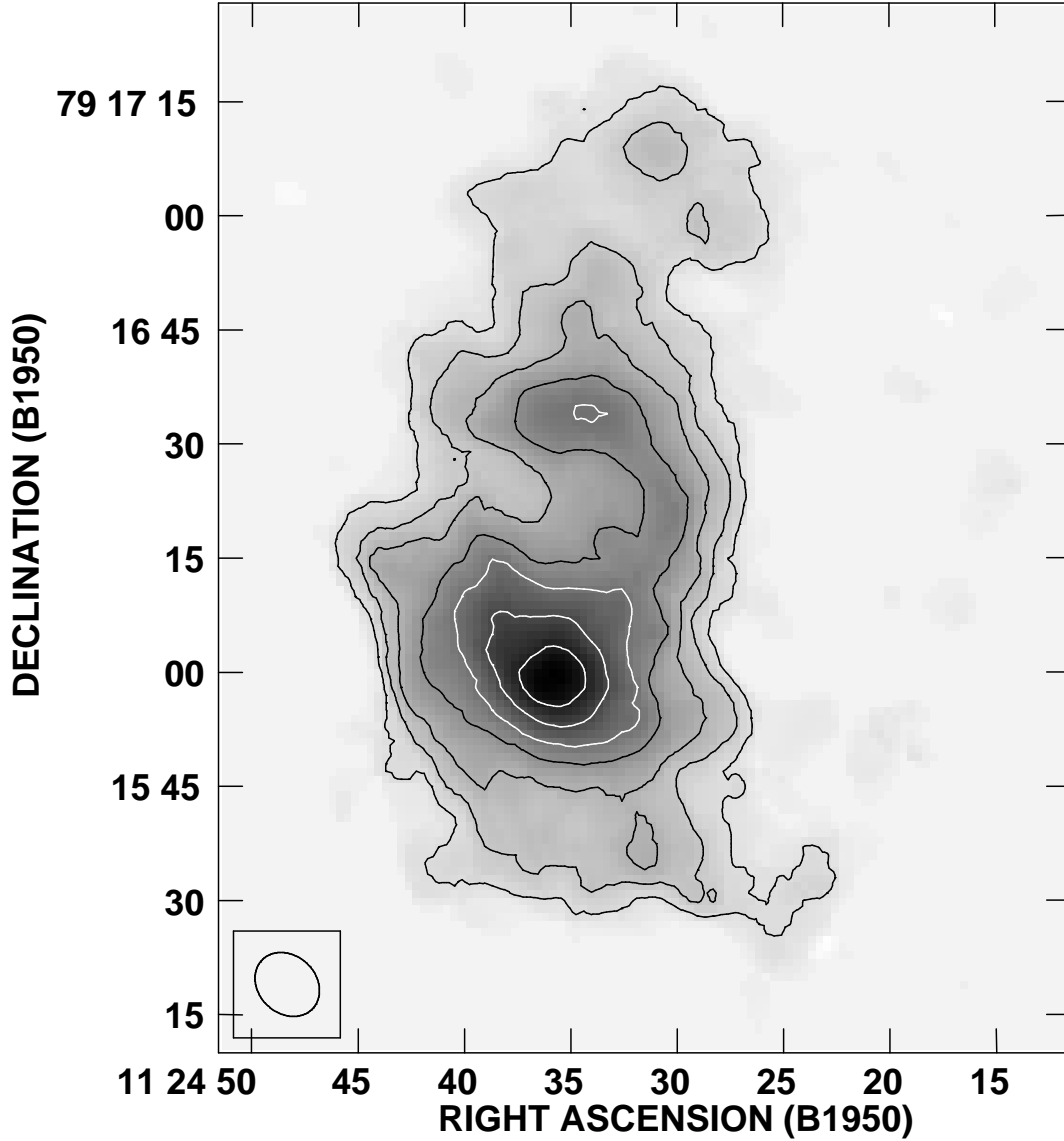
Fig. 10.— Integrated flux density map from the B+C+D$_0$ configuration data. The beam size is indicated in the lower left corner. The contour levels are (5, 10, 15, 23, 30, 40, 50) $\times 10^{20}$ cm^{-2}. The lowest contour is at 2.4σ. (A single-channel 2σ detection integrated over 3 channels is equivalent to a column density of 2.12 $\times 10^{20}$ cm^{-2}, which we take as indicative of the noise level in the integrated map.) The field of view is 1.9$'$ $\times$ 2.3$'$, which corresponds to 2.4 $\times$ 2.9 kpc.
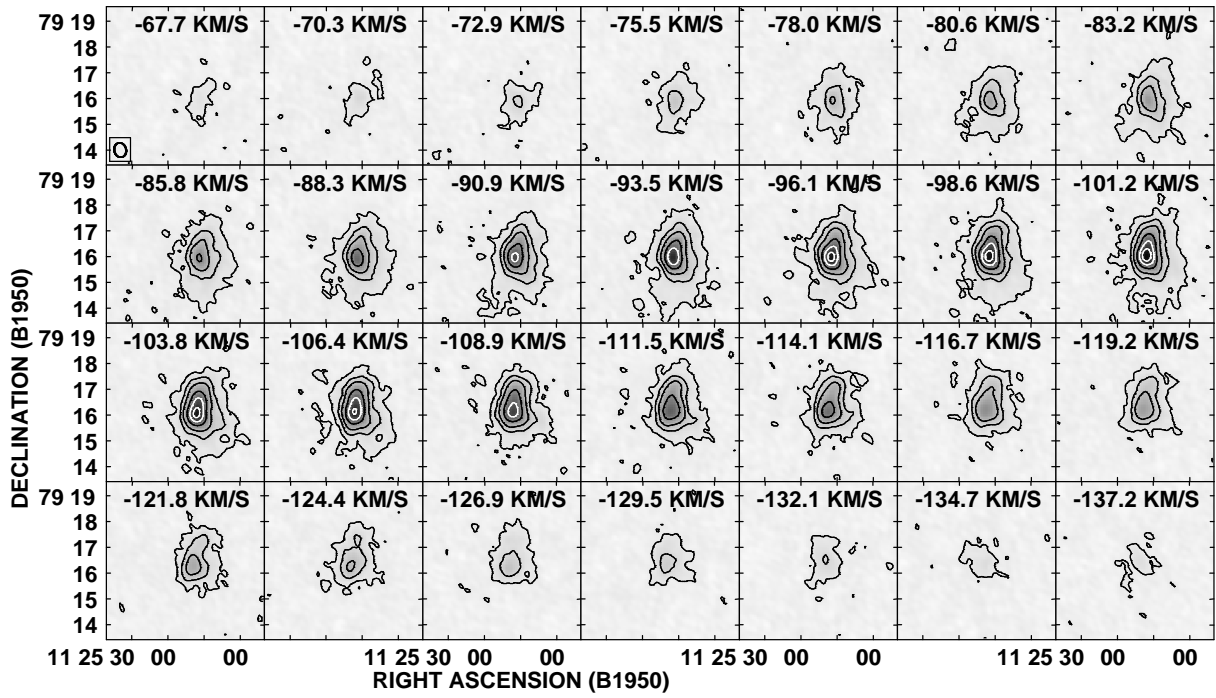
Fig. 11.— Channel maps of the H I emission in the C+D$_1$ configuration data cube. The velocity of each channel is printed along the top; the beam size is indicated in the first (top left) channel. The contours are at (3, 10, 20, 40, 60, 80, and 100) × the single-channel r.m.s. (0.83 mJy beam^{-1}).
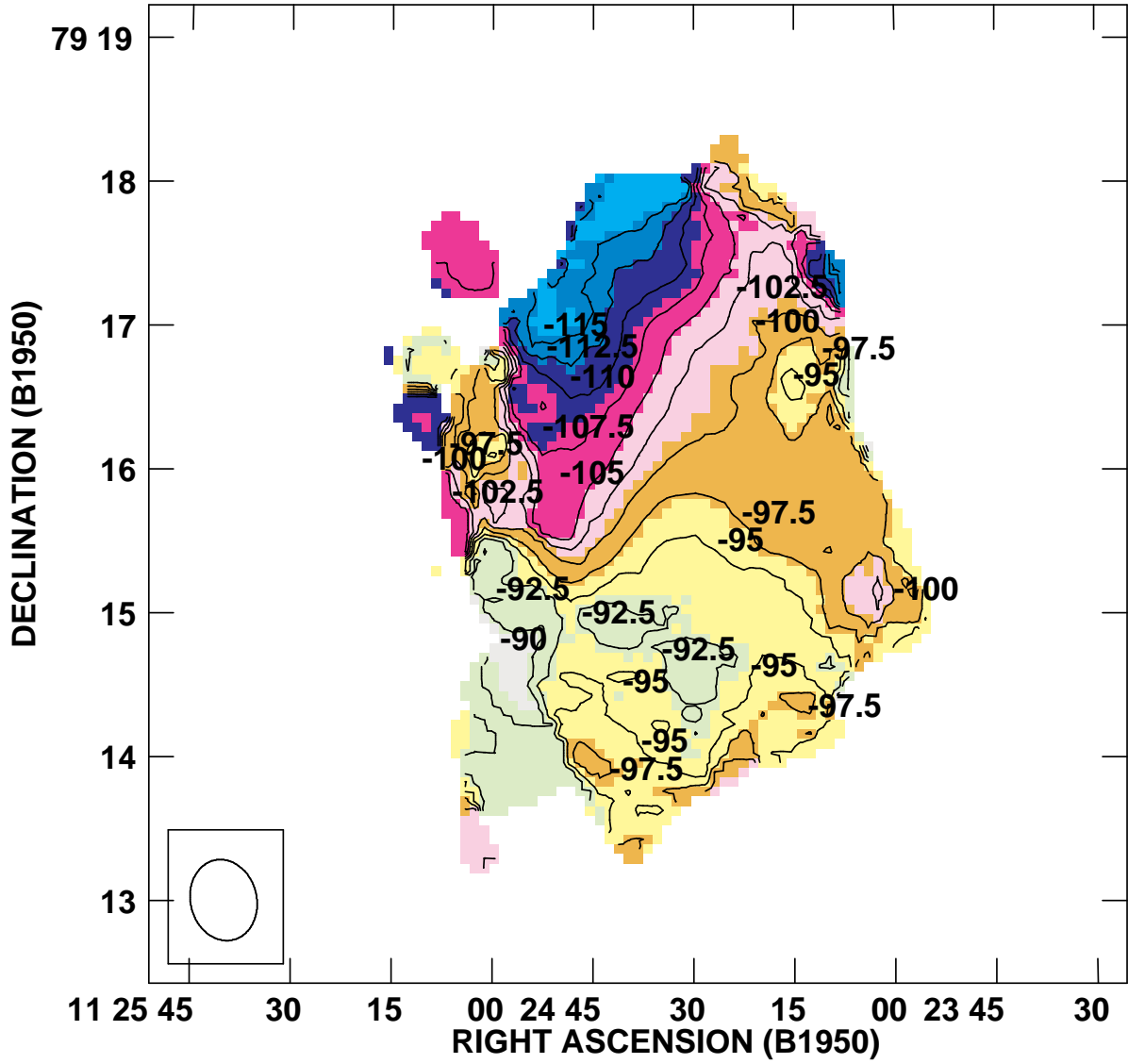
Fig. 12.— H I velocity field from the C+D$_1$ configuration data. The beam size is indicated in the lower left corner. Contours are in km s^{-1}.
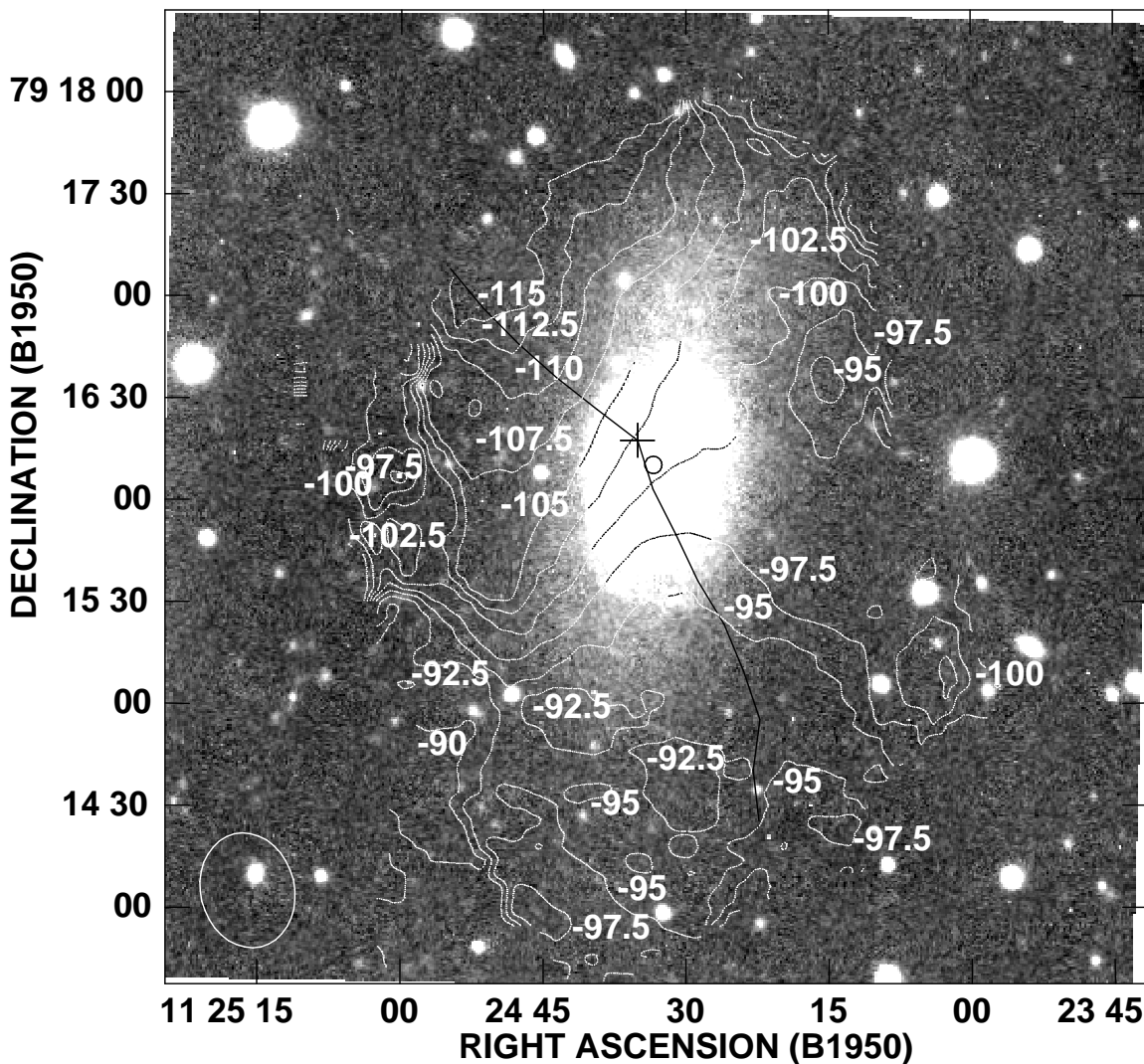
Fig. 13.— Isovelocity contours from the C+D$_1$ configuration data moment one map superposed on a V-band image of VII Zw 403. The contours, in white, are labeled with the velocity in km s^{-1}. The black line running more or less perpendicular to the isovelocity contours shows the position angle of the rotation axis in 15″ steps. The plus sign marks the kinematic center of the galaxy, and the open circle marks the center in the V-band. Note that the uncertainties on the kinematic center ($\approx 27''$) are approximately the same size as teh FWHM of the beam, which is indicated by the ellipse in the lower left corner (34.1″×27.6″). The velocity resolution is 2.6 km s^{-1}.
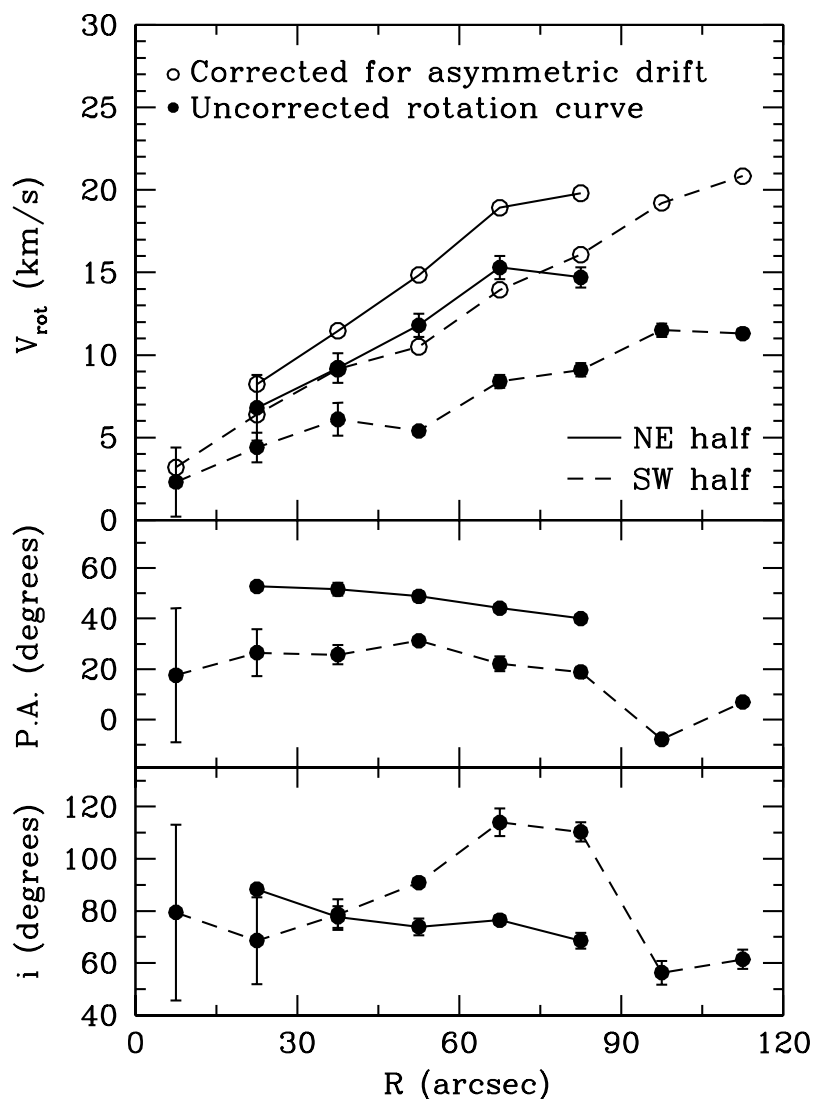
Fig. 14.— Best-fit rotation curve for VII Zw 403. The velocity field was fit in two separate parts: the NE or approaching half and the SW or receding half. Only the central position and systemic velocity were fixed in these fits, and the rotation speed, position angle, and inclination were determined in 15″ wide annuli stepped in 15″ intervals from the center. The solid symbols are the original rotation curve; the open symbols show the curve corrected for pressure support (asymmetric drift correction).
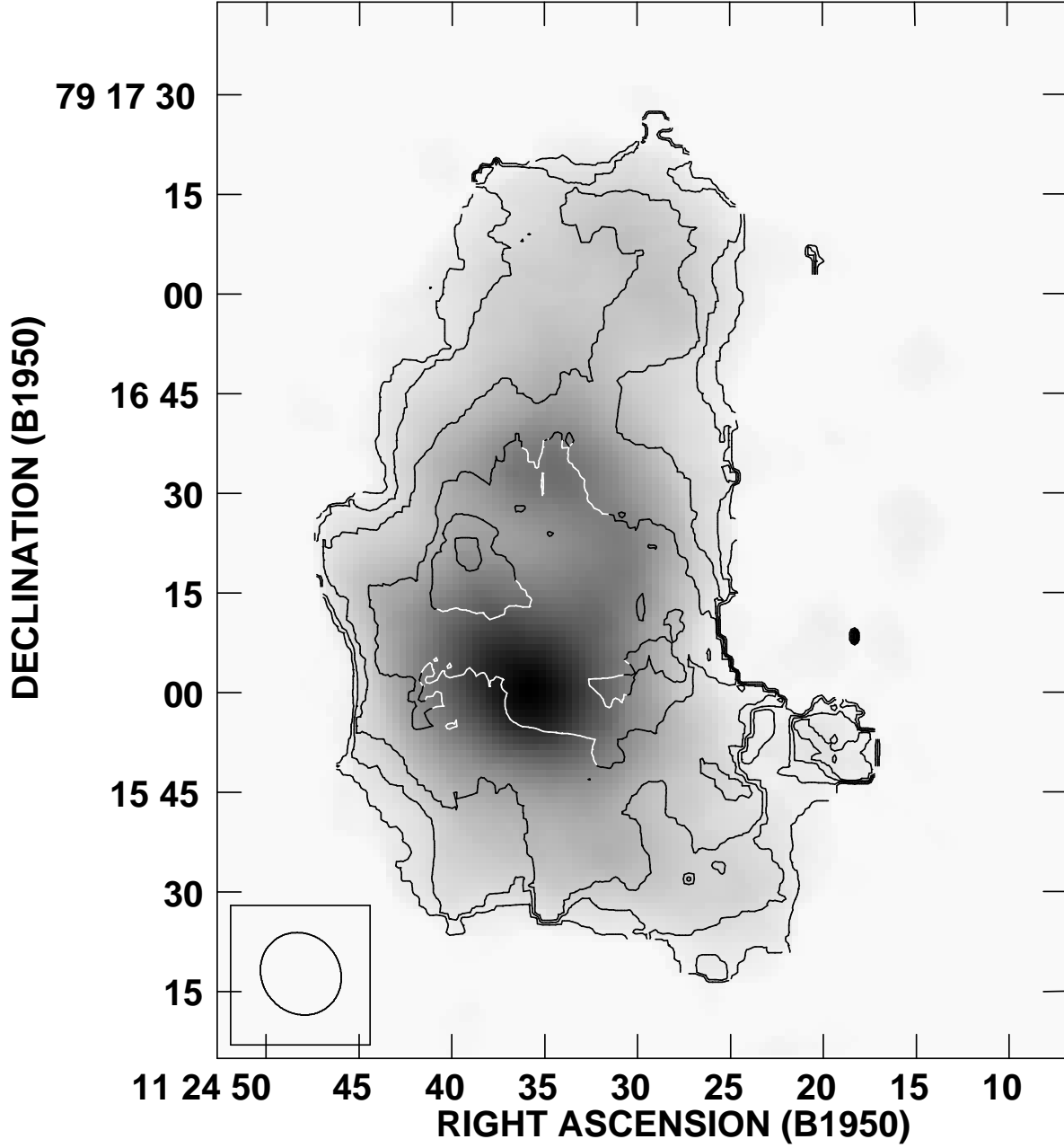
Fig. 15.— Velocity dispersion contours superposed on the integrated flux from B+C+D$_1$ data. The beam size is indicated in the lower left corner. Contours are 4, 6, 8, 10, 12, and 14 km s^{-1}.
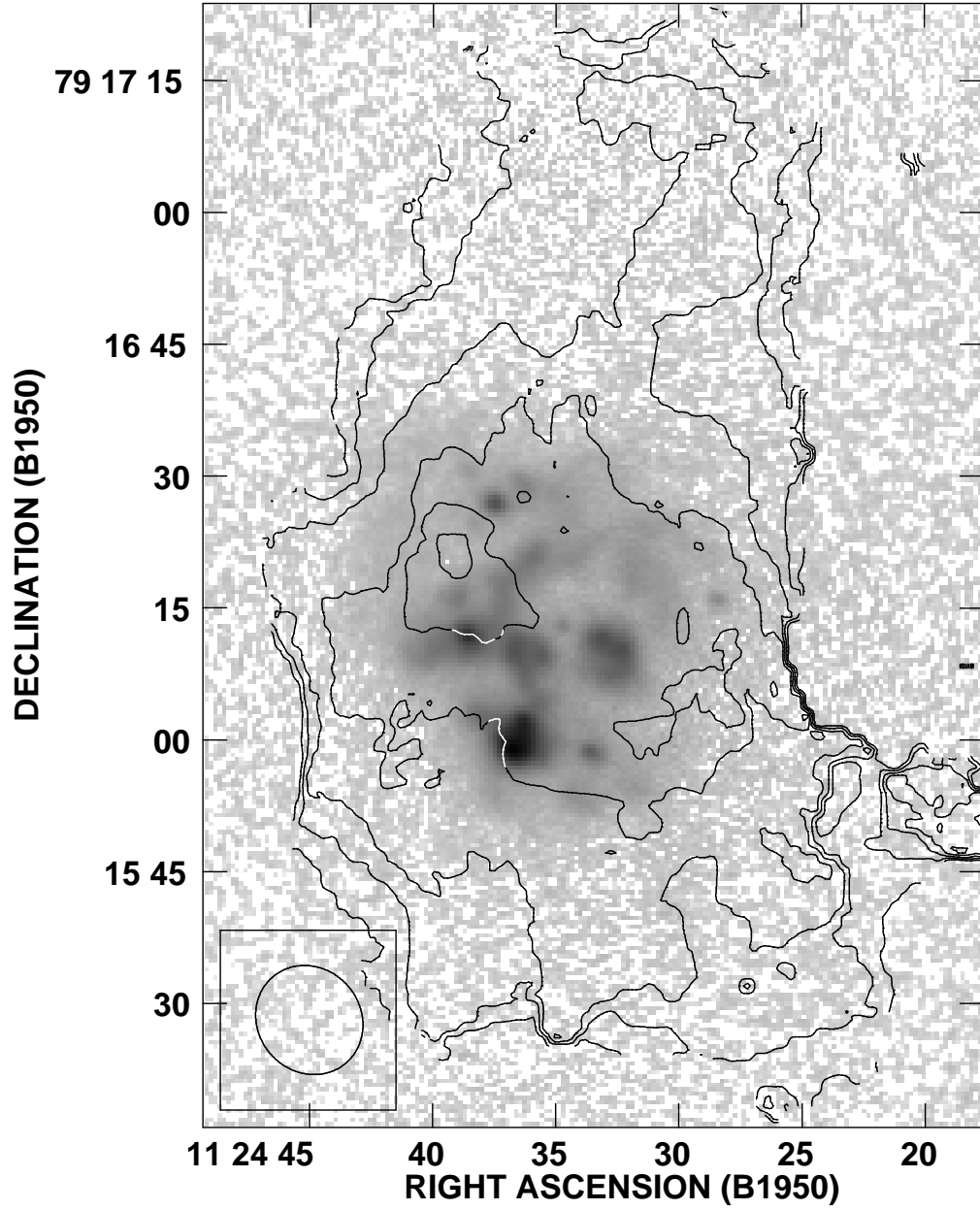
Fig. 16.— The Hα image with contours from the B+C+D$_1$ velocity dispersion map. The beam size is indicated in the lower left corner. Contour levels are 4, 6, 8, 10, 12, and 14 km s^{-1}.
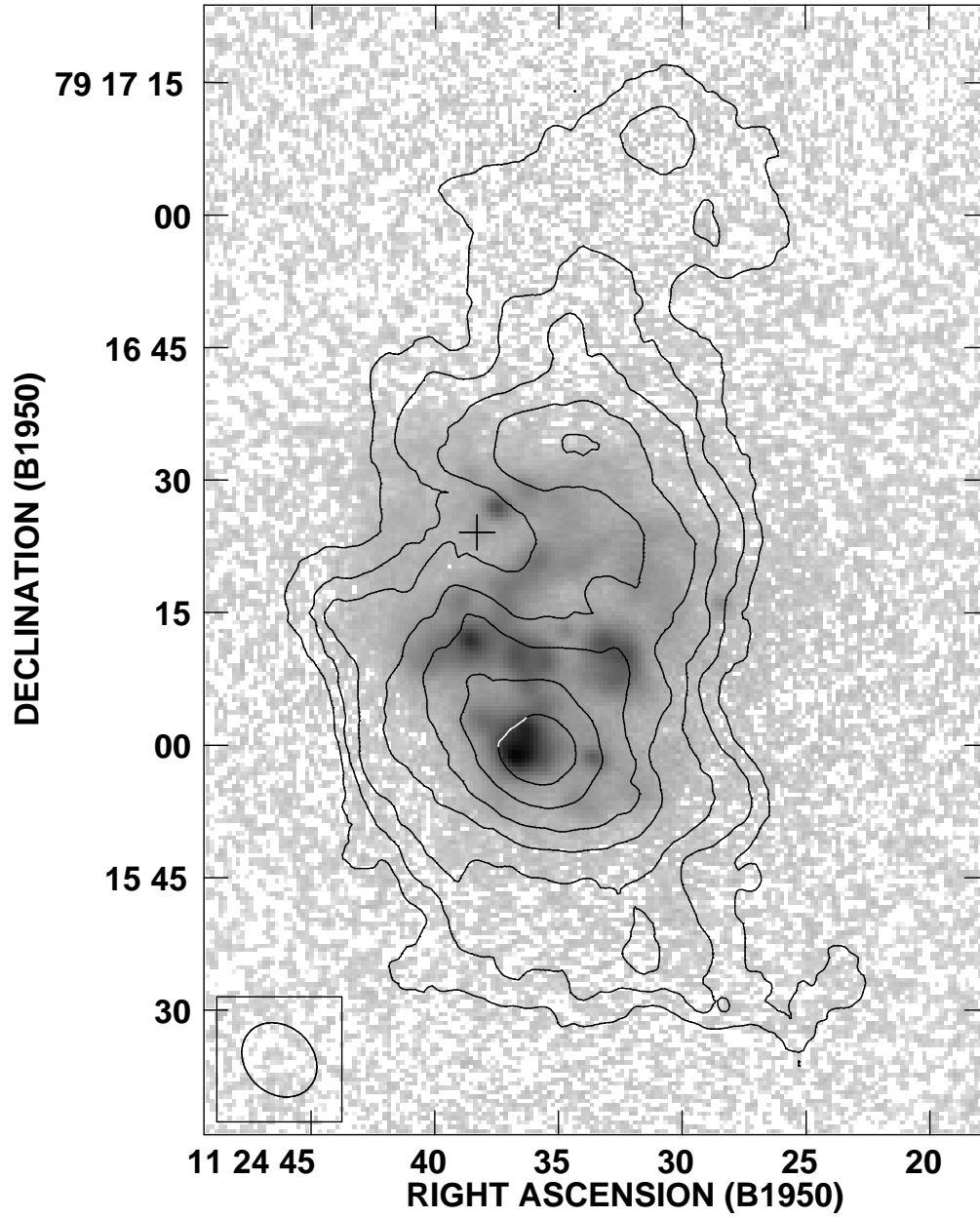
Fig. 17.— The Hα image overlaid with contours from the B+C+D₀ configuration data. The beam size is indicated in the lower left corner. The plus sign marks the location of the unresolved x-ray source detected by Ott et al. (2005a). The contour levels are the same as for Figure 10.
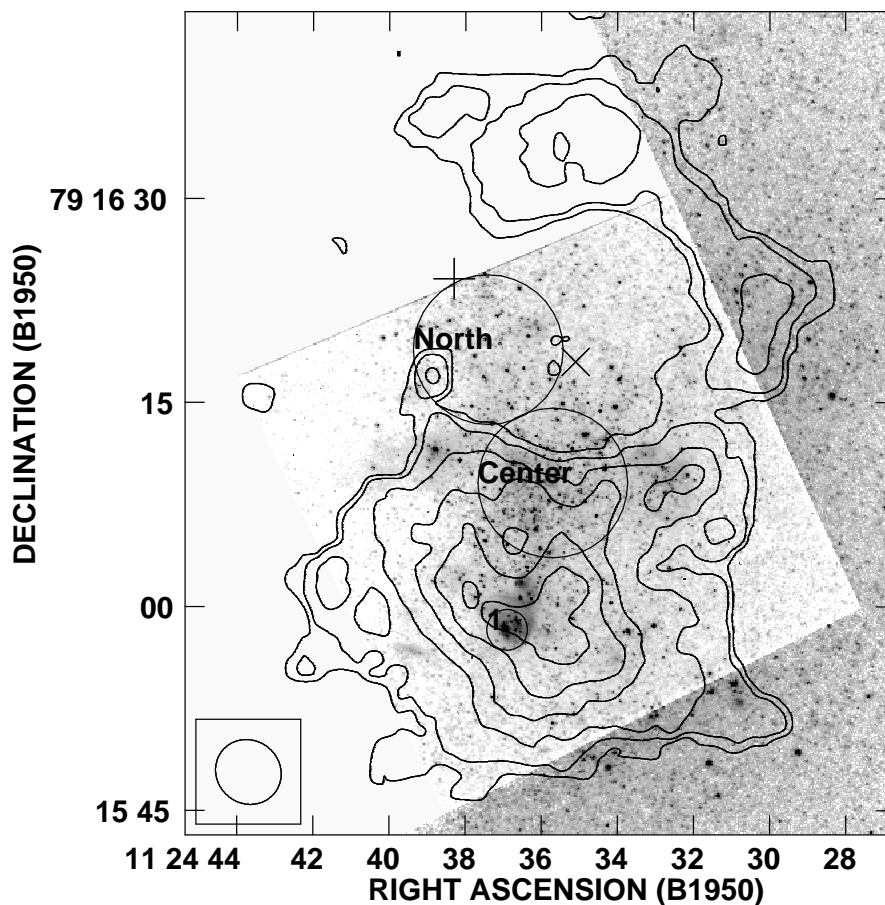
Fig. 18.— The B+C+D$_{-1}$ H I integrated flux contours on the *HST* WFPC2 image from Lynds et al. (1998). The large circles show the areas for which they determined their north and central region CMDs. The small circle labelled "1" shows the location of the brightest H II region examined by Lynds et al. (1998). The plus sign indicates the location of the unresolved x-ray source detected by Ott et al. (2005a); the $\times$ marks the location of the kinematic center as determined from the C+D$_1$ data. The beam size, shown in the lower left box, is 110×100 pc. Contours are at $(5, 10, 20, 30, 40, 50) \times 10^{20}$ cm^{-2}. The lowest contour is at 0.7σ, the second at 1.5σ. (A single-channel 2σ detection integrated over 3 channels is equivalent to a column density of 6.76×10^{20} cm^{-2}, which we take as indicative of the noise level in the integrated map.)
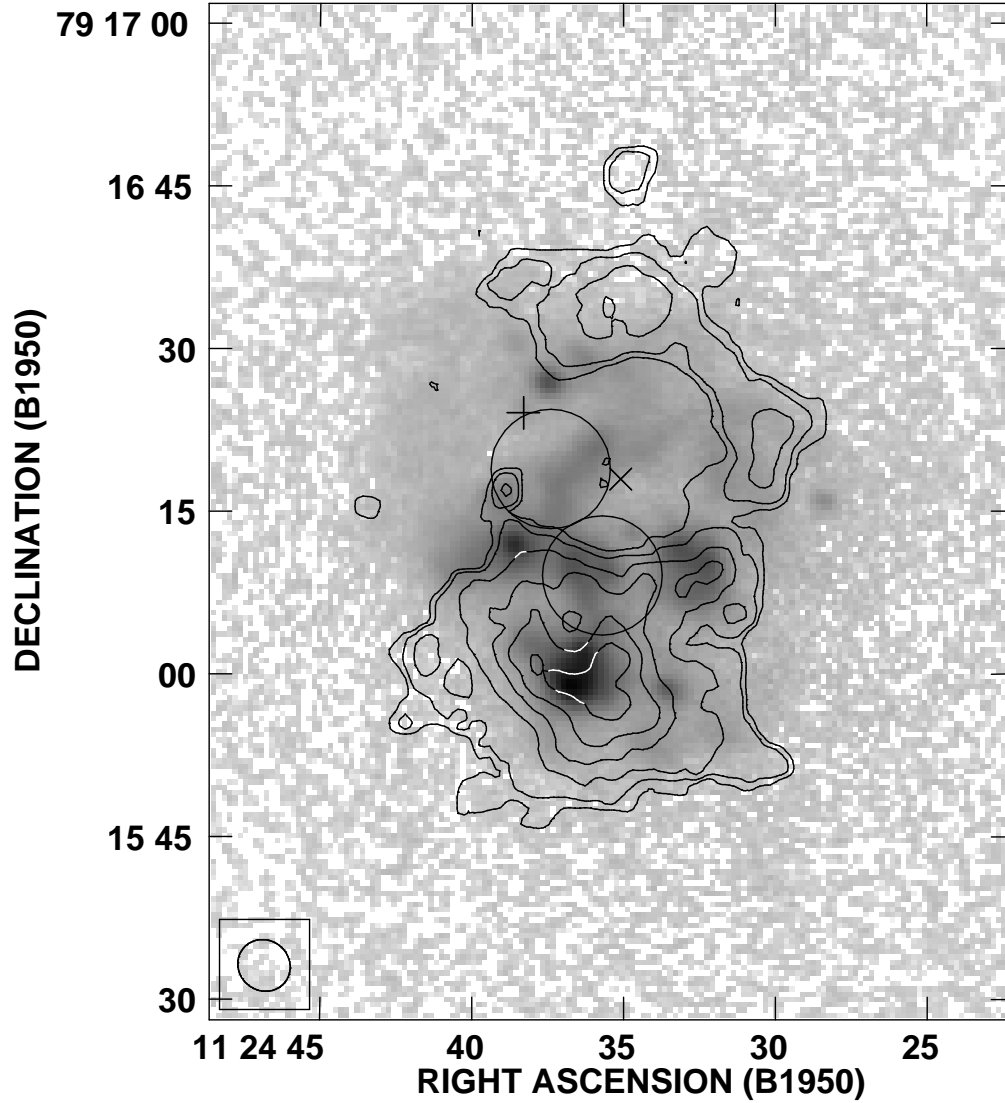
Fig. 19.— The B+C+D$_{-1}$ H I integrated flux contours on our Hα image. The circles show the areas for which Lynds et al. (1998) determined their north and central region CMDs. The plus sign indicates the location of the unresolved x-ray source detected by Ott et al. (2005a); the $\times$ marks the location of the kinematic center as determined from the C+D$_1$ data. The beam size, shown in the lower left box, is 110×100 pc. Contours are the same as for Figure 18.